Mon. Not. R. Astron. Soc. **000**, 000–000 (0000) Printed 1 February 2008 (MN LATEX style file v1.4)

The peculiar motions of early-type galaxies in two distant regions – VII. Peculiar velocities and bulk motions

Matthew Colless[1], R.P. Saglia[2], David Burstein[3], Roger L. Davies[4], Robert K. McMahan Jr.[5] and Gary Wegner[6]

[1] *Research School of Astronomy & Astrophysics, The Australian National University, Weston Creek, Canberra, ACT 2611, Australia*
[2] *Institut für Astronomie und Astrophysik, Scheinerstraße 1, D-81679 Munich, Germany*
[3] *Dept of Physics and Astronomy, Arizona State University, Tempe, AZ 85287-1504, USA*
[4] *Dept of Physics, University of Durham, South Road, Durham, DH1 3LE, UK*
[5] *Dept of Physics and Astronomy, University of North Carolina, CB#3255 Phillips Hall, Chapel Hill, NC 27599-3255, USA*
[6] *Dept of Physics and Astronomy, Dartmouth College, Wilder Lab, Hanover, NH 03755, USA*

arXiv:astro-ph/0008418v1 28 Aug 2000

Accepted —. Received —; in original form —.

ABSTRACT

We present peculiar velocities for 84 clusters of galaxies in two large volumes at distances between 6000 and 15000 $\mathrm{km\,s^{-1}}$ in the directions of Hercules-Corona Borealis and Perseus-Pisces-Cetus. These velocities are based on Fundamental Plane (FP) distance estimates for early-type galaxies in each cluster. We fit the FP using a maximum likelihood algorithm which accounts for both selection effects and measurement errors, and yields FP parameters with smaller bias and variance than other fitting procedures. We obtain a best-fit FP with coefficients consistent with the best existing determinations. We measure the bulk motions of the sample volumes using the 50 clusters with the best-determined peculiar velocities. We find the bulk motions in both regions are small, and consistent with zero at about the 5% level. The EFAR results are in agreement with the small bulk motions found by Dale et al. (1999) on similar scales, but are inconsistent with pure dipole motions having the large amplitudes found by Lauer & Postman (1994) and Hudson et al. (1999). The alignment of the EFAR sample with the Lauer & Postman dipole produces a strong rejection of a large-amplitude bulk motion in that direction, but the rejection of the Hudson et al. result is less certain because their dipole lies at a large angle to the main axis of the EFAR sample. We employ a window function covariance analysis to make a detailed comparison of the EFAR peculiar velocities with the predictions of standard cosmological models. We find the bulk motion of our sample is consistent with most cosmological models that approximately reproduce the shape and normalisation of the observed galaxy power spectrum. We conclude that existing measurements of large-scale bulk motions provide no significant evidence against standard models for the formation of structure.

Key words: galaxies: clustering — galaxies: distances and redshifts — galaxies: elliptical and lenticular, cD — galaxies: fundamental parameters — cosmology: large scale structure of universe

1 INTRODUCTION

This paper reports the main results of the EFAR project, which has measured the peculiar motions of clusters of galaxies in two large volumes at distances between 6000 and 15000 $\mathrm{km\,s^{-1}}$. The project was initiated in the wake of early studies of peculiar motions which found large-scale coherent flows over significant volumes of the local universe (Dressler et al. 1987, Lynden-Bell et al. 1988). The primary goal of the EFAR project was to test whether such large coherent motions were to be found outside the local volume within 6000 $\mathrm{km\,s^{-1}}$. In the following years, the velocity field within 6000 $\mathrm{km\,s^{-1}}$ has been mapped by several methods and in increasing detail so that today there is fair agreement on the main features of the motions (recent results are given in Giovanelli et al. 1998a,b, Dekel et al. 1999, Courteau et al. 2000, Riess 2000, da Costa et al. 2000, Wegner et al. 2000 and Tonry et al. 2000; see also the review by Dekel 2000).

© 0000 RAS

The bulk velocity within this volume, and its convergence towards the frame of reference defined by the Cosmic Microwave Background (CMB), appear to be consistent with the broad range of currently-acceptable cosmological models (Dekel 2000, Hudson et al. 2000).

However on larger scales there have been measurements of bulk motions which, at face value, appear much greater than any acceptable model would predict. The first of these was the measurement by Lauer & Postman (1994), using brightest cluster galaxies, of a bulk motion of $\sim$700 km s^{-1} towards $(l,b)\approx(340^\circ,+50^\circ)$ for a complete sample of Abell clusters out to 15000 km s^{-1}. More recently, large motions have been also be obtained for two smaller samples of clusters at similar distances, for which peculiar velocities have been measured by the more precise Fundamental Plane and Tully-Fisher estimators: Hudson et al. (1999) find a motion of 630$\pm$200 km s^{-1} towards $(l,b)=(260^\circ,-1^\circ)$ for the SMAC sample of 56 clusters at a mean distance of $\sim$8000; Willick (1999) finds a motion of 720$\pm$280 km s^{-1} towards $(l,b)=(272^\circ,+10^\circ)$ for the LP10K sample of 15 clusters at very similar distances. These two motions are in good agreement with each other, but are nearly orthogonal to the Lauer & Postman motion (though similar in amplitude). In contrast, the other extant study of peculiar motions on scales greater than 6000 km s^{-1}, the SCII Tully-Fisher survey of Dale et al. (1999a), finds a bulk flow of less than 200 km s^{-1} for a sample 52 Abell clusters with a mean distance of $\sim$11000 km s^{-1}.

At these scales the robust prediction of most cosmological models is that the bulk motion should be less than 300 km s^{-1} with about 95% confidence. It is therefore of great interest to determine whether there really are large coherent motions on scales of $\sim$10000 km s^{-1}. The EFAR peculiar motion survey probes the velocity field in the Hercules-Corona Borealis and Perseus-Pisces-Cetus regions, which are almost diametrically opposed on the sky and lie close to the axis of the bulk motion found by Lauer & Postman. With 84 clusters in these two regions extending out to $\sim$15000 km s^{-1}, the EFAR sample is well-suited to testing for this particular bulk motion. Conversely, however, it is not well-suited to testing for a bulk motion in the direction found for the SMAC and LP10K samples, which is almost orthogonal to the major axis of the EFAR sample. The main goal of this paper is to determine the peculiar motions of the EFAR clusters and the consistency of the bulk motion of the sample with both theory and other bulk motion measurements on similar scales.

The structure of this paper is as follows: In §2 we summarise the main features of the data presented in Papers I–IV of this series. In §3 we describe the maximum likelihood gaussian algorithm developed in Paper IV, which is used to determine the parameters of the Fundamental Plane and obtain the distances and peculiar velocities for the clusters. In §4 we derive the best-fitting Fundamental Plane and critically examine the random and systematic uncertainties in the fitted parameters. In §5 we derive the distances and peculiar velocities for the clusters, testing them for possible systematic biases and comparing them to the peculiar velocities obtained by other authors for the same clusters. In §6 we determine the bulk motion of the sample and compare it, using a variety of methods, to the results of other studies and to theoretical expectations. Our conclusions are given in §7.

We use H_0=50 km s^{-1} Mpc and q_0=0.5 unless otherwise specified. All redshifts and peculiar velocities are given in the CMB frame of reference.

2 THE EFAR SAMPLE AND DATA

Earlier papers in this series have described in detail the selection of the clusters and galaxies in the EFAR sample (Wegner et al. 1996, Paper I), the spectroscopic data (Wegner et al. 1999, Paper II; Colless et al. 1999, Paper V), the photoelectric and CCD photometry (Saglia et al. 1997a, Paper III; Colless et al. 1993) and the photometric fitting procedures (Saglia et al. 1997b, Paper IV; Saglia et al. 1993). In this section we briefly summarise the main properties of the EFAR database.

The clusters of galaxies in the EFAR sample are selected in two large, distant (i.e. non-local) volumes: Hercules-Corona Borealis (HCB, 40 clusters, including Coma) and Perseus-Pisces-Cetus (PPC, 45 clusters). These regions were chosen because they contain two of the richest supercluster complexes (excluding the Great Attractor/Shapley supercluster region) within 20000 km s^{-1}. The clusters come from the ACO catalogue (Abell et al. 1989), the list of Jackson (1982) and from scans of Sky Survey prints by the authors. The nominal redshift range spanned by the clusters is 6000 km s^{-1}<cz<15000 km s^{-1}. The distribution of the EFAR clusters on the sky is shown in Figure 2 of Paper I; their distribution with respect to the major supercluster complexes is shown in Figure 3 of Paper I.

Galaxies were selected in each cluster for their apparently elliptical morphology on Sky Survey prints, and for large apparent diameter. The total sample includes 736 early-type galaxies in the 85 clusters. Apparent diameters were measured visually for all early-type galaxies in the cluster fields. The range in apparent visual diameter (D_W) is from about 10 arcsec to over 60 arcsec. The sample selection function is defined in terms of these visual diameters; in total, D_W was measured for 2185 early-type galaxies in the cluster fields. Selection functions are determined separately for each cluster, and are approximated by error functions in $\log D_W$. The mean value of the visual diameter is $\langle \log D_W \rangle$=1.3 (i.e. 20 arcsec), and the dispersion in $\log D_W$ is 0.3 dex (see Paper I).

We obtained 1319 spectra for 714 of the galaxies in our sample, measuring redshifts, velocity dispersions and the Mgb and Mg$_2$ Lick linestrength indices (Paper II). There are one or more repeat observations for 45% of the sample. The measurements from different observing runs are calibrated to a common zeropoint or scale before being combined, yielding a total of 706 redshifts, 676 velocity dispersions, 676 Mgb linestrengths and 582 Mg$_2$ linestrengths. The median estimated errors in the combined measurements are Δcz=20 km s^{-1}, $\Delta\sigma/\sigma$=9.1%, ΔMgb/Mgb=7.2% and ΔMg$_2$=0.015 mag. Comparison of our measurements with published datasets shows no systematic errors in the redshifts or velocity dispersions and only small zeropoint corrections to bring our linestrengths onto the standard Lick system.

We have assigned sample galaxies to our target clus-

ters (or to fore/background clusters) by examining both the line-of-sight velocity distributions and the projected distributions on the sky (Paper II). The velocity distributions were based on EFAR and ZCAT (Huchra et al. 1992) redshifts for galaxies within $3\,h_{50}^{-1}$ Mpc of the cluster centres. These samples were also used to derive mean redshifts and velocity dispersions for the clusters. The original selection was effective in choosing cluster members, with 88% of the galaxies with redshifts being members of sample clusters and only 12% lying in fore/background clusters or the field. The median number of galaxies per cluster is 6.

We obtained R-band CCD photometry for 776 galaxies (Paper III) and B and R photoelectric photometry for 352 galaxies (Colless et al. 1993). Comparison of the CCD and photoelectric photometry shows that we have achieved a common zero-point to better than 1%, and a photometric precision of better than 0.03 mag per measurement. Circularised galaxy light profiles were fitted with seeing-convolved models having both an $R^{1/4}$ bulge and an exponential disk (Paper IV). We find that only 14% of the galaxies in our sample are well fitted by pure $R^{1/4}$ bulges and only about 1% by pure exponential disks, with most of the sample requiring both components to achieve a good fit. From these fits we derive total R-band magnitudes m_T, D_n diameters (at 20.5 mag arcsec^{-2}), half-luminosity radii R_e, and average effective surface brightnesses $\langle SB_e \rangle$, for 762 galaxies. The total R magnitudes span the range m_T=10.6–16.0 ($\langle m_T \rangle$=13.85), the diameters span D_n=4.8–90 arcsec ($\langle D_n \rangle$=20 arcsec), and the effective radii R_e span 1.6–71 arcsec ($\langle R_e \rangle$=6.9 arcsec). For 90% of our sample the precision of the total magnitudes and half-luminosity radii is better than 0.15 mag and 25% respectively. The errors on the combined quantity $FP = \log R_e - 0.3\langle SB_e \rangle$ which enters the Fundamental Plane equation are always smaller than 0.03 dex. The visual selection diameters D_W correlate well with the D_n diameters (or, equivalently, with the Fundamental Plane quantity *FP*).

The morphological type classifications of the galaxies, based on all the information available to us, reveal that 31% of the sample objects, visually selected from photographic images to be of early type, are in fact spiral or barred galaxies. The 69% of galaxies classified as early-type can be subdivided into 8% cD galaxies, 12% E galaxies (best-fit by a pure $R^{1/4}$ profile), and 48% E/S0 galaxies (best-fit by a disk plus bulge model).

All the EFAR project data is available from NASA's Astrophysical Data Centre (http://adc.gsfc.nasa.gov) and the Centre de Données astronomiques de Strasbourg (http//:cdsweb.u-strasbg.fr). A summary table with all the main parameters for every galaxy in the EFAR sample is available at these locations as J/MNRAS/*vol*/*page*. The contents of the summary table are described here in Table 1.

3 MAXIMUM LIKELIHOOD GAUSSIAN METHOD

We use a maximum likelihood gaussian algorithm for fitting the FP and determining relative distances and peculiar velocities. This algorithm, which is described in detail in Paper VI, was developed in order to deal with the general deficiencies of previous approaches and with some specific problems posed by the selection effects and measurement errors in the EFAR sample. Previous methods for fitting the FP using forms of multi-linear regression have not fully dealt with the intrinsic distribution of galaxies in size, velocity dispersion and surface brightness, nor with the simultaneous presence of measurement errors with a wide range of values in all of these quantities. The maximum likelihood gaussian algorithm properly accounts for all these factors, and also handles complex selection effects in a straightforward way. The selection criteria for the EFAR sample are well-determined, and involve both the original sample selection based on galaxy size and *a posteriori* limits imposed on both galaxy size and velocity dispersion. A specific problem with the data is that the velocity dispersion measurements include a significant fraction of cases where the errors, though themselves well-determined, are large relative to the actual value. There is also the fact that the numbers of galaxies observed per cluster are relatively small, so a method is required which is both efficient and robust against outliers (either unusual galaxies or errors in the data). The extensive simulations carried out in Paper VI demonstrate that the maximum likelihood gaussian method is superior to any of the classical linear regression approaches, minimising both the bias and the variance of the fitted parameters, and performing well in recovering the FP parameters and peculiar velocities when presented with simulations of the EFAR dataset.

The maximum likelihood gaussian method assumes that each galaxy i is drawn from an underlying gaussian distribution in the three-dimensional FP-space ($r \equiv \log R_e, s \equiv \log \sigma, u \equiv \langle SB_e \rangle$). We also assume that this underlying distribution is the same for each cluster j, apart from a shift δ_j in the distance-dependent quantity r resulting from the cluster's peculiar motion. We want to determine the mean values $(\overline{r}, \overline{s}, \overline{u})$ and the variance matrix V which characterise the galaxy distribution, along with the shifts δ_j due to the clusters' peculiar velocities. We do this by maximising the likelihood of the observed galaxy data over these parameters, while properly accounting for all the various selection effects.

The probability density for the ith galaxy, in terms of $\vec{x}_i = (r_i - \overline{r} + \delta_j, s_i - \overline{s}, u_i - \overline{u})$, is

$$P(\vec{x}_i) = \frac{\exp\left[-\frac{1}{2}\vec{x}_i{}^T (V + E_i)^{-1} \vec{x}_i\right]}{(2\pi)^{3/2} |V + E_i|^{1/2} f_i} \Theta(A\vec{x}_i - \vec{x}_{\rm cut}) \ , \qquad (1)$$

where V is the variance matrix of the underlying distribution and E_i is the error matrix of the measured quantities. The errors are convolved with the intrinsic dispersion of the galaxy distribution to give the observed distribution of the data. The exclusion function $\Theta(\vec{y}) = \prod \theta(y)$, where $\theta(y) = 1$ if $y \geq 0$ and 0 otherwise, accounts for parts of FP-space that are inaccessible because of selection effects. For simplicity, we assume that these selection effects apply to linear combinations of the variables, described by the matrix A. The normalisation factor f_i is such that $\int P(\vec{x})\, d^3x = 1$, and accounts for the selection effects described the exclusion function Θ. The likelihood of the observed sample is

$$\mathcal{L} = \prod_i P(\vec{x}_i)^{1/S(\vec{x}_i)} \ , \qquad (2)$$

where $S(\vec{x}_i)$ is the selection function giving the probability of selecting a galaxy with parameters $\vec{x}_i$. In order to correct for

Table 1. Description of EFAR summary data table.

Column	Code	Description [units]
1	GIN	Galaxy Identification Number
2	CID	Cluster Identification (see Paper I)
3	CAN	Cluster Assignment Number (see Paper II)
4	Clus	Cluster Name (corresponds to CID)
5	Gal	Galaxy Name
6	RAh	Right Ascension (J2000) [hours]
7	RAm	Right Ascension (J2000) [minutes]
8	RAs	Right Ascension (J2000) [seconds]
9	Decd	Declination (J2000) [degrees]
10	Decm	Declination (J2000) [minutes]
11	Decs	Declination (J2000) [seconds]
12	l	Galactic longitude [degrees]
13	b	Galactic latitude [degrees]
14	Type	Morphological type
15	D_n	Diameter enclosing a mean R-band SB of 20.5 mag arcsec^{-2} [arcsec]
16	δD_n	Error in D_n [arcsec]
17	$D_n(20)$	Diameter enclosing a mean R-band SB of 20.0 mag arcsec^{-2} [arcsec]
18	$D_n(19.25)$	Diameter enclosing a mean R-band SB of 19.25 mag arcsec^{-2} [arcsec]
19	R_e	Half-luminosity radius in the R-band [arcsec]
20	R_e(kpc)	Half-luminosity radius in the R-band [kpc, H_0=50, q_0=0.5]
21	SB$_e$	R-band surface brightness at R_e [mag arcsec^{-2}]
22	δSB$_e$	Photometric zero-point error on SB$_e$ [mag arcsec^{-2}]
23	$\langle SB_e \rangle$	Mean R-band surface brightness inside R_e [mag arcsec^{-2}]
24	$\delta\langle SB_e \rangle$	Photometric zero-point error on $\langle SB_e \rangle$ [mag arcsec^{-2}]
25	m_T	Total apparent R magnitude [mag]
26	δm_T	Photometric zero-point error on m_T [mag]
27	R_{eB}	Bulge half-luminosity radius in the R-band [arcsec]
28	SB$_{eB}$	Bulge R-band surface brightness at R_{eB} [mag arcsec^{-2}]
29	h	Disk scale-length in the R-band [arcsec]
30	μ_0	Disk central surface brightness in the R-band [mag arcsec^{-2}]
31	h/R_{eB}	Ratio of bulge half-luminosity radius to disk scale-length
32	D/B	Disk-to-bulge ratio (ratio of luminosity in disk to luminosity in bulge)
33	Fit	Type of fit (B=bulge, D=disk, BD=bulge+disk; other, see Paper III)
34	P	Quality of the photometric zero-point (P=0 good, P=1 bad; see Paper III)
35	Q	Global quality of the photometric fit (1=best, 2=fair, 3=poor; see Paper III)
36	$B-R$	$B-R$ colour [mag]
37	$\delta(B-R)$	Error in $B-R$ colour [mag]
38	$\langle\epsilon(R_e)\rangle$	Mean ellipticity inside R_e
39	A_R	Reddening in the R-band
40	cz_{cl}	Cluster mean redshift [km s^{-1}]
41	δcz_{cl}	Error in cz_{cl} [km s^{-1}]
42	cz	Galaxy redshift [km s^{-1}]
43	δcz	Error in cz [km s^{-1}]
44	σ	Central velocity dispersion of galaxy [km s^{-1}]
45	$\delta\sigma$	Error in σ [km s^{-1}]
46	Mgb	Mgb Lick linestrength index [Å]
47	δMgb	Error in Mgb [Å]
48	Mg$_2$	Mg$_2$ Lick linestrength index [mag]
49	δMg$_2$	Error in Mg$_2$ [mag]
50	Q_s	Spectral quality (A=best, ..., E=worst; see Paper II)
51	a/e	Absorption/emission flag
52	$\log D_W$	Logarithm of the D_W diameter [arcsec]
53	$S(D_W)$	Selection probability computed using D_W (see §3)
54	$\log D_W(D_n)$	Logarithm of D_W computed from D_n (see §3) [arcsec]
55	$S(D_W(D_n))$	Selection probability computed from $D_W(D_n)$ (see §3)

The summary table is available as J/MNRAS/*vol*/*page* from NASA's Astrophysical Data Centre (ADC, http://adc.gsfc.nasa.gov) and from the Centre de Données astronomiques de Strasbourg (CDS, http://cdsweb.u-strasbg.fr).

the selection function, each object in the sample is included in the likelihood product as if it were $1/S(\vec{x}_i)$ objects.

The error matrix can be computed from the estimated errors $(\delta r_i, \delta s_i, \delta FP_i, \delta ZP_i)$, where δFP is the error in the combined quantity $FP = r - \alpha u$ (with $\alpha \approx 0.3$) and δZP is the photometric zeropoint error. In terms of these quantities, the error matrix for galaxy i is

$$E_i = \begin{pmatrix} \delta r_i^2 & 0 & \frac{(1+\alpha^2)\delta r_i^2 - \delta FP_i^2}{\alpha(1+\alpha^2)} \\ 0 & \delta s_i^2 & 0 \\ \frac{(1+\alpha^2)\delta r_i^2 - \delta FP_i^2}{\alpha(1+\alpha^2)} & 0 & \delta u_i^2 \end{pmatrix} . \quad (3)$$

Note that δs_i combines the estimated random errors in the velocity dispersion measurements and the correlated errors between galaxies introduced by the uncertainties in calibrating dispersions obtained in different observing runs to a common system (see Paper II). Likewise, δu_i is given by the quadrature sum of the error on the effective surface brightness (from the fit to the galaxy's surface brightness distribution) and the photometric zeropoint error (see Paper III).

$$\delta u_i^2 = \frac{(\alpha^2-1)\delta FP_i^2 + (1+\alpha^2)\delta r_i^2}{\alpha^2(1+\alpha^2)} + \delta ZP_i^2 \quad (4)$$

For the EFAR sample, the selection function depends on galaxy diameter and varies from cluster to cluster (see Paper I). For galaxy i, a member of cluster j, the selection probability is

$$S_i = S(\log D_{Wi}) = \frac{1}{2}\left(1 + \mathrm{erf}\left[\frac{\log D_{Wi} - \log D^0_{Wj}}{\delta_{Wj}}\right]\right) . \quad (5)$$

The selection function for cluster j is characterised by D^0_{Wj}, the size at which the selection probability is 0.5, and by δ_{Wj}, the width of the cutoff in the selection function. For early-type galaxies, the visually estimated diameter D_{Wi} correlates with the measured diameter D_{ni} according to the relation $\log D_{ni} = 0.80 \log D_{Wi} + 0.26$, with a scatter of 0.09 dex in $\log D_{ni}$ (see Paper III). Because the visual diameters given in Paper I are individually uncertain, in computing selection probabilities we actually use an estimate of D_{Wi} obtained by inverting this relation and inserting the accurately measured value of D_{ni}.

In order to avoid biasing the FP fits and the estimated peculiar velocities, it would be desirable to sample the same part of the FP galaxy distribution in all clusters. However, because the clusters are at different redshifts, the approximately constant apparent diameter selection limit corresponds to actual diameter selection limits D^0_{Wj} for the clusters that vary by about a factor of 2–3 (the approximate range of cluster redshifts; see Paper 1). We can limit this redshift-dependent sampling bias by excluding the smaller galaxies, which are only sampled in the nearer clusters. Guided by the simulations of Paper VI, we choose a selection limit $D_{W\mathrm{cut}}$=12.6 kpc. This choice balances the reduced bias of a higher $D_{W\mathrm{cut}}$ against the larger sample size of a lower $D_{W\mathrm{cut}}$ (95% of galaxies in the EFAR sample have $D_{Wi} \geq 12.6$ kpc). Because of the good correlation between D_{Wi} and the combined quantity $FP = r - 0.3u$ (see Paper III), this cut in D_{Wi} corresponds to an approximate selection limit $FP_{\mathrm{cut}} \approx 0.78 \log D_{W\mathrm{cut}} - 6.14 \approx -5.28$.

Another selection limit is due to the difficulty of measuring velocity dispersions smaller than a spectrograph's instrumental resolution. For the spectrograph setups we used, only velocity dispersions greater than about $100\,\mathrm{km\,s^{-1}}$ could be reliably measured (see Paper II). We therefore impose a limit s_{cut}=2, excluding galaxies with $\sigma < 100\,\mathrm{km\,s^{-1}}$. The overall exclusion function for the EFAR sample is thus $\Theta = \theta(s - s_{\mathrm{cut}})\theta(FP - FP_{\mathrm{cut}})$.

The mean of the distribution, $(\overline{r},\ \overline{s},\ \overline{u})$, the variance matrix V, and the shifts δ_j, are all determined by minimising $-\ln\mathcal{L}$, which for the EFAR sample is given by

$$-\ln\mathcal{L} = \sum_{FP>FP_{\mathrm{cut}}}^{s>s_{\mathrm{cut}}} S_i^{-1}\left[0.5\vec{x}_i{}^T(V+E_i)\vec{x}_i + 0.5\ln|V+E_i| + \ln f_i\right] \quad (6)$$

(where the constant term $1.5\ln(2\pi)$ has been dropped).The normalisation f_i is obtained by integrating the gaussian distribution over the accessible volume defined by $s>s_{\mathrm{cut}}$ and $FP>FP_{\mathrm{cut}}$. The minimisation is performed using the simplex algorithm (Press et al., 1986).

The FP is defined as the plane $r = as + bu + c$ that passes through $(\overline{r},\ \overline{s},\ \overline{u})$ and whose normal is the eigenvector of V with the smallest eigenvalue. For convenience, we define the second axis of the galaxy distribution to be the unit vector within the FP that has zero coefficient for s (in fact, this turns out to be a reasonable approximation to one of the remaining eigenvectors of V). The three unit vectors giving the axes of the galaxy distribution can then be written in terms of the FP constants as

$$\begin{aligned} \hat{v}_1 &= \hat{r} - a\hat{s} - b\hat{u} \\ \hat{v}_2 &= \hat{r} + \hat{u}/b \\ \hat{v}_3 &= -\hat{r}/b - (1+b^2)\hat{s}/(ab) + \hat{u} , \end{aligned} \quad (7)$$

where $\hat{r}$, $\hat{s}$, and $\hat{u}$ are the unit vectors in the directions of the FP-space axes. The eigenvalues of V give the dispersions σ_1, σ_2 and σ_3 of the galaxy distribution in the directions of the eigenvectors; the smallest eigenvalue, σ_1, is the intrinsic dispersion of the galaxies about the FP.

The final step of the process is to recover each cluster's distance and peculiar velocity. The mean galaxy size, $\overline{r} \equiv \overline{\log R_e}$, provides a standard scale which we can use to determine relative distances and peculiar velocities. The offset δ_j between the true mean galaxy size, $\overline{\log R_e}$, and the mean galaxy size observed for cluster j, $\overline{\log R_e} - \delta_j$, is a measure of the ratio of the true angular diameter distance of a cluster, D_j, to the angular diameter distance corresponding to its redshift, $D(z_j)$:

$$\frac{D_j}{D(z_j)} = \frac{\mathrm{dex}(\overline{\log R_e})}{\mathrm{dex}(\overline{\log R_e} - \delta_j)} = 10^{\delta_j} . \quad (8)$$

The relation between angular diameter distance and redshift (Weinberg 1972) is given by

$$D(z) = \frac{cz}{H_0(1+z)^2} \frac{1 + z + \sqrt{1+2q_0 z}}{1 + q_0 z + \sqrt{1+2q_0 z}} . \quad (9)$$

We assume H_0=50 $\mathrm{km\,s^{-1}}$ Mpc, q_0=0.5, and compute all redshifts and peculiar velocities in the CMB frame of reference. The peculiar velocity of the cluster, V_j, is then obtained as

$$V_j = \frac{cz_j - cz(D_j)}{1 + z(D_j)}, \quad (10)$$

where $z(D_j)$ is the redshift corresponding to the true distance D_j through the inverse of equation (9). Note that we are not using the low-redshift approximation $V = cz -$

$H_0D = cz(1-10^{\delta})$, which leads to small but systematic errors in the peculiar velocities (e.g., at cz=15000 km s^{-1}, the approximation leads to a systematic peculiar velocity error of about -4%).

These distances and peculiar velocities are relative, because the standard scale is determined by assuming that the distance (or, equivalently, peculiar velocity) of some standard cluster (or set of clusters) is known. Distances and peculiar velocities are therefore in fact relative to the true distance and peculiar velocity of this standard.

4 THE FUNDAMENTAL PLANE

4.1 Best-fit solution and random errors

We determine the parameters of the Fundamental Plane and the cluster peculiar velocities in a two-step process. We first fit the Fundamental Plane using only those clusters with 6 or more suitable galaxies having reliable dispersions, effective radii and mean surface brightnesses (the criteria are given below). We exclude clusters with fewer members because the simulations of Paper VI show that including less well-sampled clusters increases the variance on the FP parameters. We then determine peculiar velocities for *all* the clusters in a second step, where we fix the FP parameters at the values determined in the first step. This procedure results in more accurate and precise peculiar velocities than a simultaneous global solution for the FP parameters and the peculiar velocities.

In order to be included in the fit a galaxy had to satisfy the following criteria: (1) good quality photometric fit (Q=1 or Q=2; see Paper III); (2) $\sigma \geq 100$ km s^{-1} and $\delta \log \sigma \leq 0.5$ (see Paper II); (3) a selection diameter $D_W \geq 12.6$ kpc and a selection probability $\geq$0.1. The first criterion excludes galaxies with unreliable structural and photometric parameters (see Paper III); the second excludes galaxies with dispersions less that the typical instrumental resolution or which have very large uncertainties; the third ensures that the clusters have uniform selection criteria and that no individual galaxy enters with a very high weight. No galaxy is excluded on the basis of its morphological type. There were 31 clusters in the sample with 6 or more galaxies satisfying these criteria.

As well as these *a priori* criteria, we also rejected a further 8 galaxies on the basis that they lie outside *both* the 3-σ ellipse of the galaxy distribution in the *FP*–$\log\sigma$ plane when the FP fit is obtained using all the galaxies in these 31 clusters meeting the selection criteria (including themselves), *and* outside the 5-σ ellipse of the galaxy distribution when the FP fit is obtained excluding them. These galaxies are listed in Table 2, which gives their galaxy ID number (GIN), their cluster assignment number (CAN), their EFAR name, their morphological type and, where appropriate, their NGC/IC numbers. The reasons why these 8 galaxies are poorly fitted by the FP distribution that satisfactorily represents the other 255 galaxies fulfilling the selection criteria are not apparent. Although three are spirals, the other five include two ellipticals, two E/S0s and a cD. Three are members of A2151, including the cD NGC 6041. Two of these galaxies (GINs 45 and 370) are in clusters with data for 6 members; these two clusters (A160 and A1983) therefore drop out of the sample of clusters to which we fit the FP. Also listed in Table 2 are another 3 galaxies in clusters with fewer than 6 members that are excluded from further analysis because they lie outside the 5-σ ellipse of the best-fitting galaxy distribution.

Table 2. Galaxies excluded from the Fundamental Plane fits.

GIN	CAN	Name	Type	NGC/IC
(i) Galaxies in clusters with ≥6 members				
45	7	A160 C	E/S0	
167	21	A400 H	E/S0	
370	43	A1983 2	S	
396	46	J16-W B	S	
456	53	A2147 D	E	
495	58	A2151 A	cD	N6041
500	58	A2151 F	S	I1185
501	58	A2151 G	E	I1193
(ii) Galaxies in clusters with <6 members				
355	42	J14-1 D	S	
489	57	J18 C	E	
552	63	A2162-S G	E/S0	

The final sample of 29 clusters used to fit the FP parameters is listed in Table 3, which gives the cluster assignment number (CAN), the cluster name, the mean heliocentric redshift and the number of galaxies that enter the FP fit. Of these 29 clusters, 12 are in HCB and 17 in PPC. They span the redshift range 6942 km s^{-1} (Coma) to 20400 km s^{-1} (A419), though most are in the range 9000–15000 km s^{-1}. However, they have similar selection diameters D_W^0, with minimum values of the D_W diameter in the range $\log D_W$(kpc)=1.0–1.3. The Coma cluster sample is supplemented with the data of Müller (1997; see also Müller et al. 1998, 1999), which were obtained using essentially the same methodology. Müller's photometric data have been adjusted by adding 0.04 mag in order to bring them into agreement with the EFAR data for galaxies in common.

In fitting the FP we assume H_0=50 km s^{-1} Mpc^{-1} and q_0=0.5. We fix the zeropoint of the FP by forcing the mean of the FP shifts of the 29 clusters to be zero—i.e. we fix $\overline{\log R_e}$ by requiring $\sum \delta_j$=0. This results in a peculiar velocity for Coma of only -29 km s^{-1}, so our FP zeropoint is essentially identical to that obtained by setting the peculiar velocity of Coma to be zero, as is often done. The effective radii and mean surface brightnesses used were the total R_e and $\langle SB_e \rangle$ (rather than the bulge-only R_{eB} and $\langle SB_{eB} \rangle$) given in Paper III. In applying absorption corrections (taken to be $2.6E_{\rm B-V}/4.0$) we have adopted the mean of the absorption corrections derived from Burstein & Heiles (1982, 1984; BH) and Schlegel et al. (1998, SFD; with $E_{\rm B-V}$ offset by -0.02 mag, the mean offset from BH given by SFD). The above assumptions and cluster/galaxy selection criteria yield our best fit to the FP. This best fit is given as case 1 in Table 4, which lists the number of clusters and galaxies in the fit, the FP coefficients a, b and c, and the means and dispersions describing the galaxy distribution: $\overline{\log R_e}$, $\overline{\log \sigma}$, $\overline{\langle SB_e \rangle}$, σ_1, σ_2 and σ_3. The table also explores the effects of the various assumptions and selection criteria, giving the FP fits obtained for a wide range of alternative cases.

Case 1 is our best-fit solution. The EFAR FP, based on 29 clusters and 255 galaxies, has a=1.223±0.087, b=0.336±0.013 and c=−8.66±0.33. The intrinsic scatter

Table 4. The parameters of the Fundamental Plane derived for various cases.

Case	$N_{\rm cl}$	$N_{\rm gal}$	a	b	c	$\overline{\log R_e}$	$\overline{\log\sigma}$	$\overline{\langle SB_e\rangle}$	σ_1	σ_2	σ_3	Notes
1	29	255	1.223	0.3358	−8.664	0.7704	2.304	19.71	0.0638	1.995	0.6103	standard fit
2	29	271	1.286	0.3439	−8.975	0.7621	2.298	19.72	0.0688	1.958	0.6201	includes Q=3 photometry
3	29	261	1.201	0.3265	−8.430	0.7840	2.306	19.74	0.0671	2.057	0.6202	includes rejected galaxies
4	29	255	1.232	0.3373	−8.721	0.7686	2.300	19.73	0.0642	1.992	0.6138	uses BH absorption corrections
5	29	255	1.183	0.3292	−8.422	0.7961	2.315	19.69	0.0632	2.019	0.5901	uses SFD absorption corrections
6	29	255	1.220	0.3349	−8.639	0.7739	2.306	19.71	0.0638	1.996	0.6043	uses 0.64SFD+0.36BH corrections
7	29	235	1.235	0.3357	−8.690	0.7750	2.300	19.74	0.0642	2.014	0.6161	excludes $\delta\log\sigma$>0.1
8	29	255	1.082	0.3221	−8.062	0.8159	2.329	19.74	0.0612	2.057	0.5394	no D_W cut is applied
9	29	275	1.132	0.3224	−8.184	0.7773	2.297	19.73	0.0675	2.122	0.6827	$D_{W\,\rm cut}$=6.3 kpc
10	29	244	1.300	0.3388	−8.906	0.7446	2.292	19.69	0.0637	2.040	0.6220	$D_{W\,\rm cut}$=14.1 kpc
11	29	222	1.247	0.3303	−8.607	0.7369	2.265	19.74	0.0696	2.001	0.7176	$D_{W\,\rm cut}$=15.9 kpc
12	29	255	1.077	0.3014	−7.665	0.7511	2.310	19.66	0.0458	1.575	0.5286	excludes galaxies with $\ln\mathcal{L}$<0
13	29	256	1.207	0.3359	−8.625	0.7725	2.299	19.72	0.0625	1.981	0.6326	uses q_0=0
14	29	258	1.204	0.3472	−8.846	0.6745	2.206	19.77	0.0634	1.965	0.8923	uses galaxies with S_i>0.01
15	29	241	1.080	0.3239	−8.081	0.8099	2.315	19.73	0.0575	2.135	0.6276	uses galaxies with S_i>0.2
16	29	255	1.221	0.3309	−8.553	0.8302	2.331	19.75	0.0646	2.108	0.5981	uses no selection weighting
17	29	255	1.223	0.3345	−8.629	0.7895	2.305	19.73	0.0637	2.001	0.6091	mean FP shift set to +0.01
18	29	255	1.215	0.3342	−8.628	0.7700	2.307	19.73	0.0636	1.999	0.6056	mean FP shift set to −0.01
19	29	255	1.227	0.3359	−8.648	0.7990	2.302	19.71	0.0639	1.991	0.6136	mean FP shift set to +0.03
20	29	255	1.226	0.3359	−8.704	0.7418	2.303	19.71	0.0639	1.992	0.6104	mean FP shift set to −0.03
21	29	255	1.227	0.3374	−8.707	0.7735	2.304	19.72	0.0639	2.249	0.4334	also fit third axis of FP
22	29	255	1.247	0.3341	−8.694	0.7721	2.301	19.75	0.0564	2.192	0.6402	uses uniform errors for all galaxies
23	66	397	1.206	0.3274	−8.452	0.8021	2.307	19.77	0.0634	2.051	0.6619	uses clusters with $N_{\rm gal}\geq$3
24	52	355	1.208	0.3272	−8.460	0.7969	2.306	19.78	0.0644	2.035	0.6564	uses clusters with $N_{\rm gal}\geq$4
25	39	304	1.244	0.3265	−8.531	0.7927	2.306	19.77	0.0651	2.084	0.6139	uses clusters with $N_{\rm gal}\geq$5
26	31	265	1.228	0.3329	−8.616	0.7839	2.305	19.74	0.0643	1.994	0.6060	uses clusters with $N_{\rm gal}\geq$6
27	16	173	1.109	0.3432	−8.525	0.7487	2.299	19.59	0.0661	1.765	0.5890	uses clusters with $N_{\rm gal}\geq$8
28	7	99	0.992	0.3526	−8.425	0.7652	2.326	19.52	0.0544	1.864	0.5564	uses clusters with $N_{\rm gal}\geq$10
29	29	222	1.330	0.3351	−8.904	0.7776	2.320	19.68	0.0668	2.009	0.5470	excludes spirals
30	66	348	1.284	0.3327	−8.737	0.8186	2.330	19.73	0.0660	1.966	0.5488	excludes spirals; $N_{\rm gal}\geq$3
31	52	310	1.293	0.3323	−8.756	0.8097	2.330	19.72	0.0675	1.947	0.5404	excludes spirals; $N_{\rm gal}\geq$4
32	39	267	1.352	0.3291	−8.835	0.7966	2.323	19.72	0.0678	2.006	0.5452	excludes spirals; $N_{\rm gal}\geq$5
33	31	232	1.333	0.3300	−8.804	0.8020	2.322	19.73	0.0673	2.027	0.5414	excludes spirals; $N_{\rm gal}\geq$6
34	29	223	1.147	0.3198	−8.174	0.7558	2.300	19.68	0.0646	1.861	0.6102	excludes cD galaxies
35	29	199	1.241	0.3125	−8.250	0.7568	2.319	19.62	0.0672	1.831	0.5426	excludes spirals and cDs

about this FP is σ_1=0.064±0.006, corresponding in to an intrinsic error in estimating distances of 15%⋆. Figure 1a shows the projection of the galaxy distribution in the $\log\sigma$–FP plane (where $FP = r - bu$). The hard cut in $\log\sigma$ and the approximate cut in FP are indicated by dashed lines. The shape of the best-fitting galaxy distribution is shown by the projections of its major and minor axes and its 1, 2, 3 and 4-σ contours. Figure 1b shows the scatter of $\log R_e$ about the FP predictor for $\log R_e$, namely $a\log\sigma + b\langle SB_e\rangle + c$. The rms scatter about the 1-to-1 relation (the solid line) is 0.087 dex, which is larger than σ_1 because of the errors in the measurements. (Allowing for the estimated measurement errors, the reduced χ^2 is 1.01, which is a consistency check on the fitted value of σ_1.) Thus although the intrinsic rms precision of distance estimates from the FP is 0.064 dex (15%), the effective rms precision for the EFAR sample when the intrinsic scatter and the measurement errors are combined is 0.087 dex (20%).

The random errors given above for the best-fit parameters are based on 1000 simulations of the recovery of the FP from the EFAR dataset (assuming *no* peculiar velocities) using the maximum likelihood gaussian algorithm, as described in Paper VI. Figure 2 shows the distributions of the fitted parameters from these 1000 simulations: the dotted vertical line is the input value of the parameter and the smooth curve is the gaussian with the same mean and rms as the fits. There are residual biases in the fitted parameters, as shown by the offsets between the input parameters and the mean of the fits: a is biased low by 6%, b is biased low by 2%, c is biased high by 4%; $\overline{\log R_e}$, $\overline{\log\sigma}$and $\overline{\langle SB_e\rangle}$are all biased high, by 0.036 dex, 0.007 dex and 0.05 mag respectively; the scatter about the FP is under-estimated by 0.006 dex, or 1.4%. These biases are all less than or comparable to the rms width of the distribution, so that although they are statistically significant (i.e. much greater than the standard error in the mean, rms/$\sqrt{1000}$), they do not dominate the random error in the fitted parameters. We do not correct for these biases since they are small and have negligible impact on the derived distances and peculiar velocities (see §5 below).

⋆ Logarithmic errors, ϵ, are converted to linear errors, ε, according to $\varepsilon = (10^{+\epsilon} - 10^{-\epsilon})/2$.

4.2 Variant cases and systematic errors

All the other cases listed in Table 4 are variants of this standard case, as briefly described in the Notes column of Table 4. Case 2 includes galaxies with poorer quality (Q=3) photometry and less reliable structural parameters, increas-

Table 3. The Fundamental Plane cluster sample.

CAN	Name	cz ($\mathrm{km\,s^{-1}}$)	N_{FP}
1	A76	11888	6
3	A119	13280	6
10	J30	15546	6
13	A260	10944	8
16	J8	9376	8
17	A376	14355	7
20	A397	9663	8
21	A400	7253	6
23	A419	20400	6
24	A496	9854	6
25	J34	11021	8
34	A533	14488	6
35	A548-1	11866	19
36	A548-2	12732	6
39	J13	8832	8
46	J16W	11321	7
48	A2040	13455	6
50	A2063	10548	9
53	A2147	10675	10
58	A2151	11106	10
59	J19	12693	7
65	A2197	9137	9
66	A2199	9014	9
68	A2247	11547	7
70	J22	10396	10
80	A2593-N	12399	18
82	A2634	9573	12
83	A2657	12252	7
90	Coma	6942	20

ing the scatter about the FP. Case 3 includes the outlier galaxies rejected from the standard sample, and also has a larger FP scatter. Cases 4–6 show that applying alternative prescriptions for the absorption corrections (BH corrections, SFD corrections without an offset, and corrections based on a 36:64 weighting of BH and SFD) has no significant effect on the FP fit. Case 7 shows that applying a stricter constraint on the errors in the velocity dispersions, excluding galaxies for which $\delta\log\sigma>0.1$, also has no effect. Cases 8–11 correspond to different cuts in D_W (no cut and $D_{W\,\mathrm{cut}}$=6.3, 14.1 and 15.9 kpc respectively); there is a slight flattening of the FP slope a for lower cuts. Case 12 excludes not only the galaxies rejected from the standard fit, but also galaxies with low likelihoods ($\ln\mathcal{L}<0$); this results in a highly biased fit, with both a and b significantly lower than in the standard case, and with an artificially lowered FP scatter. Case 13 shows that assuming a q_0=0 cosmology has no impact on the FP fit. Cases 14 and 15 examine the effect of a lower ($S_i>0.01$) and a higher ($S_i>0.2$) limit on the allowed selection probabilities. The former case has highly deviant values for $\overline{\log R_e}$, $\overline{\log\sigma}$ and $\overline{\langle SB_e\rangle}$ due to over-weighting a few galaxies with low selection probabilities; the latter case has biased values of a, b and c due to ignoring the tail of the selection function. Case 16 ignores the selection probabilities altogether and applies a uniform weight to all galaxies, resulting in an effective over-weighting of the larger galaxies and biasing the mean values of $\overline{\log R_e}$ and $\overline{\log\sigma}$ to higher values. Cases 17–20 show that setting the mean FP shift to +0.01, −0.01, +0.03 and −0.03 dex respectively (rather than to zero, as in the standard case) has no effect on the fitted FP.

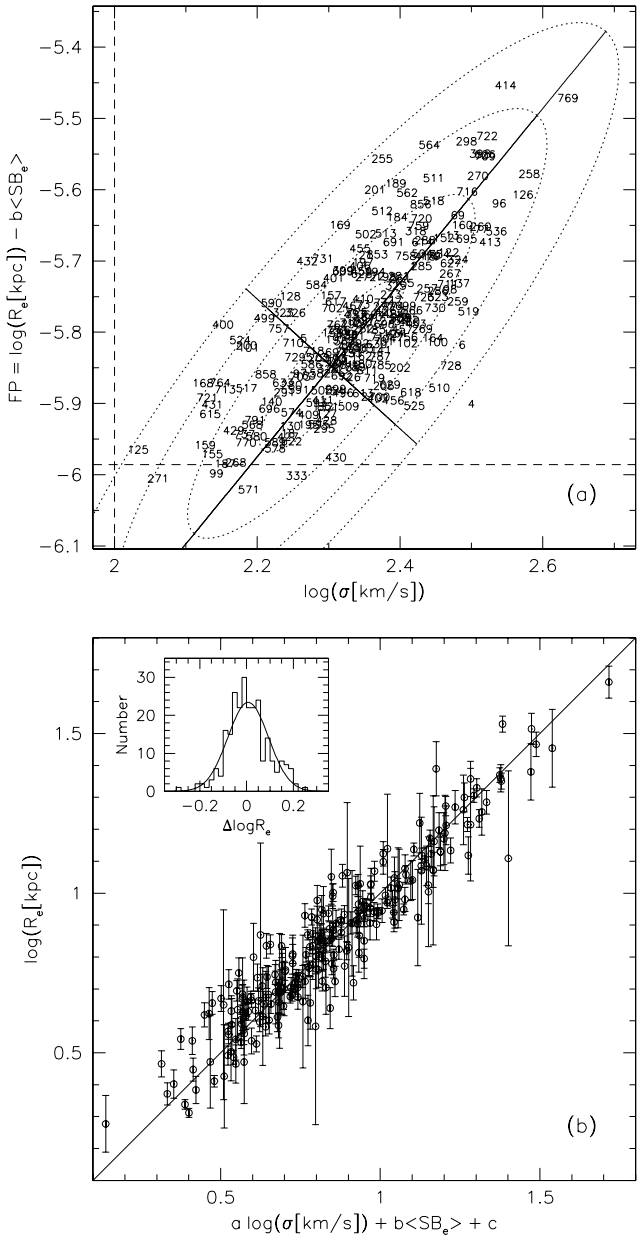

Figure 1. The best-fitting FP solution (case 1) for 255 galaxies belonging to the 29 clusters with 6 or more members. (a) The projection of the galaxies (marked by their GINs) in the $\log\sigma$–*FP* plane (where $FP = r - bu$). The dashed lines are the cut in $\log\sigma$ and the approximate cut in *FP*. The best-fitting gaussian distribution is shown by the projections of its major and minor axes and its 1, 2, 3 and 4-σ contours. (b) The scatter of $\log R_e$ about the FP predictor for $\log R_e$, namely $a\log\sigma+b\langle SB_e\rangle+c$. The rms scatter about the 1-to-1 line is 0.087 dex (an rms distance error of 20% per galaxy). The inset histogram of residuals $\Delta\log R_e$ has a gaussian with an rms of 0.087 dex overlaid.

Case 21 permits an extra degree of freedom by allowing the orientation of the major axis of the galaxy distribution *within* the FP to be fitted, rather than specified *a priori*. The unit vectors of the galaxy distribution for the standard case, given by equation (7), are

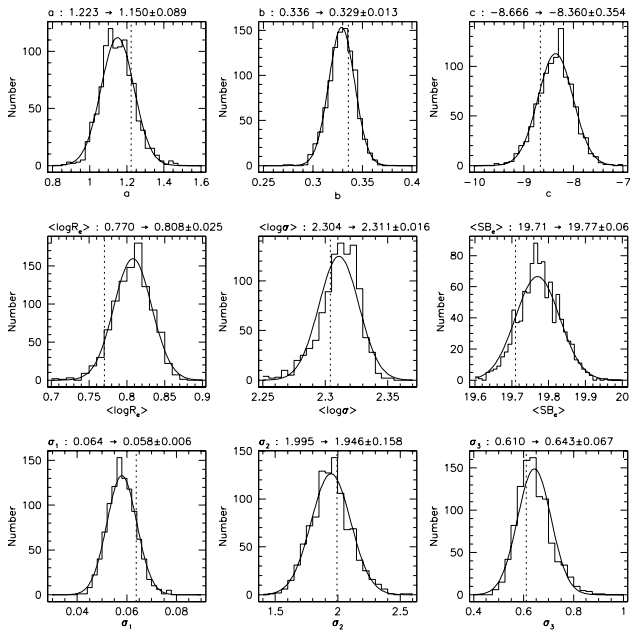

Figure 2. The distributions of the FP parameters a, b, c, $\overline{\log R_e}$, $\overline{\log \sigma}$, $\overline{\langle SB_e \rangle}$, σ_1, σ_2 and σ_3 resulting from fitting 1000 simulations of the best-fit FP. The input parameters of the simulations are given at the head of each panel (and indicated by the vertical dotted line), followed by the mean and rms of the fits to the simulations (the curve is the gaussian with this mean and rms).

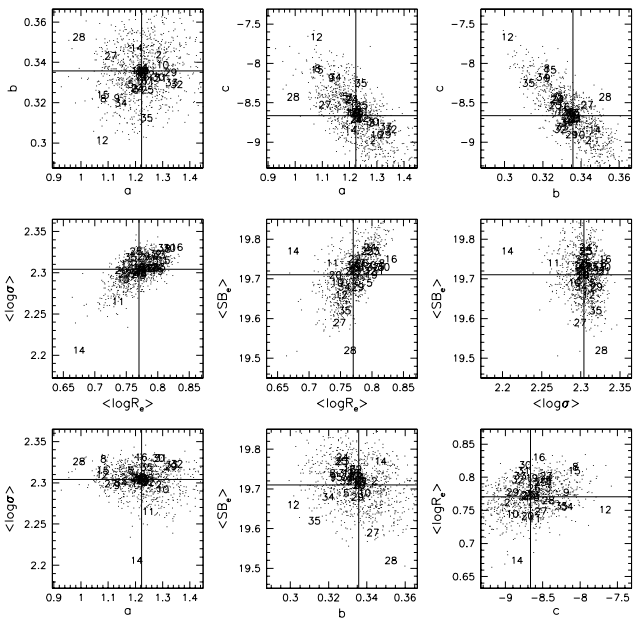

Figure 3. The fitted FP parameters for each case in Table 4, showing the distributions and correlations for various pairs of parameters. Each case is numbered as in the table. The dots are the distribution of fits obtained for 1000 simulations of the standard case after removing the effects of the residual biases.

$$\begin{aligned} \hat{v}_1 &= +1.000\hat{r} - 1.223\hat{s} - 0.336\hat{u} \\ \hat{v}_2 &= +1.000\hat{r} + 0.000\hat{s} + 2.978\hat{u} \\ \hat{v}_3 &= -2.978\hat{r} - 2.710\hat{s} + 1.000\hat{u} \ , \end{aligned} \tag{11}$$

while the true eigenvectors, obtained by fitting with the extra degree of freedom, are

$$\begin{aligned} \hat{v}_1 &= +1.000\hat{r} - 1.227\hat{s} - 0.337\hat{u} \\ \hat{v}_2 &= +1.000\hat{r} - 0.032\hat{s} + 2.964\hat{u} \\ \hat{v}_3 &= -3.176\hat{r} - 2.863\hat{s} + 1.000\hat{u} \ . \end{aligned} \tag{12}$$

The coefficient of $\hat{s}$ in the second eigenvector is small, justifying the simplifying approximation of setting it to zero used in equation (7). The FP itself is very close to the standard fit, while the axes within the FP have coefficients differing from the standard values by no more than a few percent; σ_1 stays the same, while σ_2 is maximised and σ_3 is minimised.

Case 22 replaces the individual error estimates for all measured quantities with uniform errors; this has little effect on the FP, but under-estimates the intrinsic scatter about the plane. Cases 23–28 explore the effects of varying the minimum number of galaxies required for a cluster to be included in the fit, from 3, 4, 5, 6 and 8 up to 10. Note that this is the number of galaxies in the cluster before excluding outliers; hence case 26 differs from case 1 in having 31 clusters rather than 29. The simulations of Paper VI suggested that a spuriously small estimate for σ_1 could in principle result when clusters with few galaxies are included in the fit, as offsetting the FP with a spurious peculiar velocity could suppress the apparent scatter. However this effect is not observed in fitting the actual data, and the FP fits are consistent with the errors on the best fit for samples with a minimum number of galaxies per cluster of between 3 and 8. A significantly flatter FP slope is found only for the set of clusters with 10 or more galaxies, where there are only 7 clusters and 99 galaxies in the fit and correspondingly larger uncertainties. Case 29 is the same as the standard case except that spirals are excluded, so that the FP is fitted only to galaxies with E, E/S0 and cD morphological types. The FP slope for these early-type galaxies is steeper, with a=1.33. Cases 30–33 are similar to case 29, but with the minimum number of galaxies required for a cluster to be included in the fit varied from 3 to 6. Cases 34 and 35 are the same as the standard case except that the fit is restricted, respectively, to exclude cD galaxies and both cD galaxies and spirals. Removing cDs flattens a and lowers b, in contrast to case 29; removing both cDs and spirals restores the FP to the intermediate values obtained by including both populations.

Figure 3 shows the fitted values in each case for various pairs of the parameters, in order to show their distributions and correlations. The cases are numbered following Table 4. The dots show the distribution of fits obtained for 1000 simulations of the standard case (case 1) after removing the effects of the residual biases. The main point to note is that, with only a few exceptions (noted above), the systematic differences in the fits derived for difference cases are comparable to the random errors in the determination of the parameters for the standard case. We conclude that the uncertainties in our best-fit FP parameters are dominated by the random errors and not by systematic effects from the fitting method. In particular we conclude that the following inputs have relatively little effect on the fitted FP: the absorption correction, the cosmological model, the assumed mean FP shift and the choice of the second and third FP axes. Our standard case provides an optimum fit to the FP because: (i) it excludes the galaxies with poor structural parameters

Table 5. Determinations of the Fundamental Plane.

Source	Band	A	B	Δ	Fit method
Dressler et al. (1987)	B	1.33 ± 0.05	-0.83 ± 0.03	20%	inverse
Djorgovski & Davis (1987)	r_G	1.39 ± 0.14	-0.90 ± 0.09	20%	2-step inverse
Lucey et al. (1991)	B	1.27 ± 0.07	-0.78 ± 0.09	13%	inverse
Guzmán et al. (1993)	V	1.14	−0.79	17%	forward
Jørgensen et al. (1996)	r	1.24 ± 0.07	-0.82 ± 0.02	17%	orthogonal
Hudson et al. (1997)	R	1.38 ± 0.04	-0.82 ± 0.03	20%	inverse
Scodeggio et al. (1997)	I	1.25 ± 0.02	-0.79 ± 0.03	20%	mean regression
Pahre et al. (1998)	K	1.53 ± 0.08	-0.79 ± 0.03	21%	orthogonal
Müller et al. (1998)	R	1.25	−0.87	19%	orthogonal
Gibbons et al. (2000)	R	1.39 ± 0.04	-0.84 ± 0.01	19%	inverse
EFAR (this paper)	R	1.22 ± 0.09	-0.84 ± 0.03	20%	ML gaussian

and velocity dispersion measurements which artificially inflate the scatter about the FP and the uncertainty in the FP parameters; (ii) it applies a selection function cutoff that balances over-weighting a small number of galaxies against biasing the results by ignoring galaxies with low selection probabilities; (iii) it uses clusters with 6 or more galaxies to avoid artificially reducing FP scatter by confusing scatter with peculiar velocities while yet retaining a sufficiently large overall number of galaxies to keep the random errors in the FP parameters small.

4.3 Comparison with previous work

Table 5 compares the best-fit EFAR FP with previous determinations in the literature, noting both the passband to which the relation applies and the method of the fit. To match the usage in most of this literature, we present the FP in the form $R_e \propto \sigma_0^A \langle\Sigma\rangle_e^B$, where σ_0 is the central velocity dispersion and $\langle\Sigma\rangle_e$ is the mean surface brightness (in linear units) within the effective radius R_e. The exponents of this relation are related to the coefficients of our FP relation, $\log R_e = a\log\sigma + b\langle SB_e\rangle + c$, by $A{=}a$ and $B{=}-2.5b$. The table also quotes the fractional distance error, Δ, corresponding to the rms scatter about the FP in R_e. In most cases the determination of the FP is limited to galaxies with $\sigma{>}100\,\mathrm{km\,s^{-1}}$. The forward and inverse fitting methods are linear regressions with, respectively, $\log R_e$ and $\log\sigma$ as the independent variable; orthogonal fitting minimises the residuals orthogonal to the FP, while mean regression averages the fits obtained by taking each of $\log R_e$, $\log\sigma$ and $\langle SB_e\rangle$ as the independent variable.

The first point to note is that all the fitted values of B are consistent within the errors, regardless of passband and fitting method. The second point to note is that this is not true for A, which has a higher value in the K-band FP fit of Pahre et al. (1998) than in any of the optical fits. The third point is that, within the optical FP fits, the forward and inverse fits give, respectively, lower and higher values of A than the orthogonal and mean regressions and the maximum likelihood gaussian method. This is consistent with the analysis and simulations of the methods carried out in Paper VI: for samples in which the errors in σ dominate and/or selection cuts are applied in R_e (as is the case for most of these datasets), the value of A will be under-estimated by a forward fit and over-estimated by an inverse fit. Orthogonal and mean regressions reduce these biases, with the least bias being produced with the maximum likelihood method. We conclude that apparent differences between FP fits in optical passbands are due to differences in the fitting methods that have been applied.

There is also consistency on the observed scatter about the FP as represented by the fractional distance error, Δ. With the exception of Lucey et al. (1991), the observed errors are all in the range 17% to 21%. This is consistent with (i.e. larger than) the estimated intrinsic scatter about the FP of 15% that we derive from the EFAR sample, and the range corresponds to the range of measurement errors in the various studies, which account for between 8% and 15% of the observed scatter.

5 DISTANCES AND PECULIAR VELOCITIES

In order to determine distances and peculiar velocities, we re-apply the maximum likelihood gaussian algorithm to the whole cluster sample. This time we fix the parameters of the intrinsic galaxy distribution at their best-fit values (case 1 of Table 4) and fit only for the shift of the FP for each cluster.

5.1 Sample

We remove outliers (interlopers from the cluster foreground or background, objects which genuinely do not lie on the FP, and objects with bad data) by excluding the galaxies that deviate most from the fitted FP until all clusters have FP fits with $\chi^2/\nu{<}3$. To check that this procedure is conservative, we visually inspected each cluster's distribution of $D_g - D_c$ (individual galaxy distances relative to the overall cluster distance, from the residuals about the best-fit FP) with respect to $cz_g - cz_c$ (individual galaxy redshifts relative to the overall cluster redshift). The rejected galaxies were invariably clear outliers in these distributions. In all, 36 galaxies were rejected using this procedure, including all the galaxies rejected from the FP fit (see Table 2). The list of galaxies excluded from the peculiar velocity fits is given in Table 6. There were three clusters with $\chi^2/\nu{>}3$ (CAN 2=A85 with 4 galaxies, CAN 55=P386-2 with 2 galaxies, CAN 79=A2589 with 5 galaxies) for which half or more of the galaxies had to be rejected in order to obtain a good FP fit, so that it was difficult to determine which galaxies were the outliers. Although we give distances and peculiar velocities for these clusters below (using all the available galaxies), we exclude them from further analysis.

Table 6. Galaxies excluded from the peculiar velocity fits.

GIN	CAN	Name	GIN	CAN	Name
45	7	A160 C	489	57	J18 C
52	7	A160 J	495	58	A2151 A
78	11	A193 A	500	58	A2151 F
125	16	J8 D	501	58	A2151 G
128	16	J8 G	519	59	A2152 I
156	20	A397 F	525	59	A2152 1
167	21	A400 H	552	63	A2162-S G
184	23	A419 H	562	65	A2197 A
187	23	A419 1	564	65	A2197 C
189	24	A496 A	584	66	A2199 F
200	25	J34 E	590	66	A2199 L
201	25	J34 F	711	80	A2593-S C
271	35	A548-1 F	713	80	A2593-S E
355	42	J14-1 D	721	82	A2634 F
370	43	A1983 2	728	82	A2634 2
396	46	J16-W B	730	83	A2657 B
432	50	A2063 G	731	83	A2657 C
456	53	A2147 D	756	90	COMA 133

5.2 Bias corrections

To the extent that its assumptions are justified, the maximum likelihood gaussian algorithm accounts for the effects of biases on the estimated distances which are due to the selection function of the galaxies within each cluster. (We refer to this bias as 'selection bias' rather than 'Malmquist bias' because, following the usage of Strauss & Willick (1995), the effect is due to the selection criteria and not the line-of-sight density distribution.) As discussed in Paper VI, however, the sample selection function parameter D^0_{Wj} varies with cluster redshift, introducing a redshift-dependent bias in the peculiar velocity estimates. Although this bias is reduced by the selection limit $D_{Wi}{>}D_{W\rm cut}$ imposed on galaxy sizes (see §3), clusters with $D^0_{Wj}{>}D_{W\rm cut}$ are nonetheless sampled differently to clusters with $D^0_{Wj}{\le}D_{W\rm cut}$. This difference in the way the FP galaxy distribution is sampled in different clusters leads to a residual bias in the clusters' fitted FP offsets and peculiar velocities as a function of D^0_{Wj} (or redshift, with which D^0_{Wj} is closely correlated).

This effect is investigated in detail through simulations in Paper VI. Figure 4 shows the residual selection bias determined from 1000 simulations of the EFAR dataset. For clusters with redshifts below the sample mean the bias in the peculiar velocities is small and negative, while for clusters at redshifts above the sample mean it is positive and increases rapidly with redshift. We correct this systematic bias individually for each cluster by subtracting the mean error in the FP offset determined from 1000 simulations of the EFAR dataset before computing the cluster distances and peculiar velocities. The size of the corrections are shown in the inset histograms of Figure 4. For the subsample of clusters included in subsequent analyses of the peculiar velocities (whose selection is discussed below), the amplitude of the bias correction is less than $250\,{\rm km\,s^{-1}}$ for 40 of the 50 clusters. The random errors in the peculiar velocities are typically of order $1000\,{\rm km\,s^{-1}}$, while the uncertainties in the peculiar velocity bias corrections for these clusters are typically less than $50\,{\rm km\,s^{-1}}$. To the extent that the simulated datasets match the real distribution of galaxies in the FP, therefore, the bias corrections should not significantly increase the random errors in the peculiar velocities.

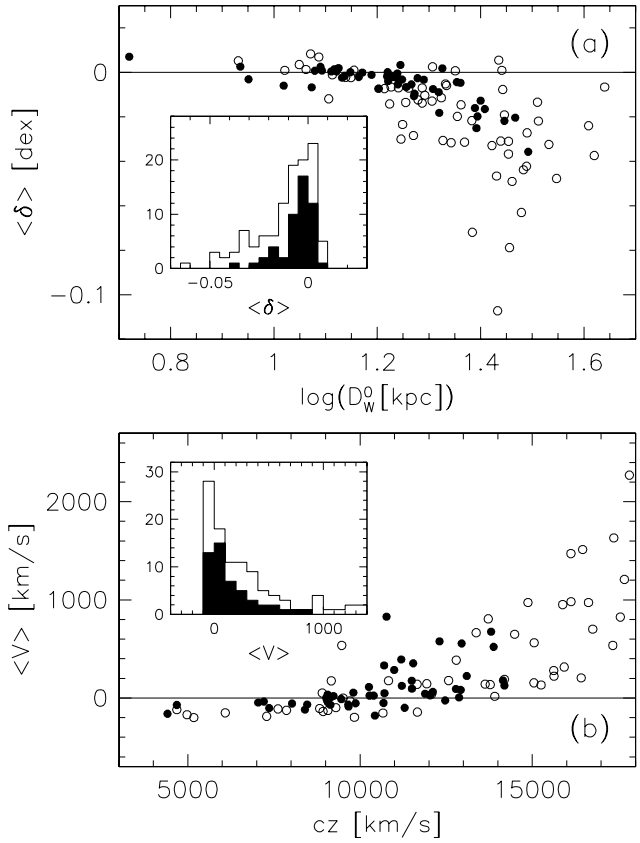

Figure 4. The residual selection bias determined from 1000 simulations of the EFAR dataset. (a) The bias in the FP offsets $\langle\delta_j\rangle$ for each cluster as a function of the cluster's selection function parameter D^0_{Wj}. The inset histogram shows the distribution of bias corrections $\langle\delta\rangle$. (b) The corresponding bias in the cluster peculiar velocities $\langle V_{\rm pec}\rangle$ as a function of cluster redshift cz. The inset histogram shows the distribution of bias corrections $\langle V_{\rm pec}\rangle$. The filled symbols and the shaded histogram show the subsample of clusters used in the peculiar velocity analysis.

5.3 Results

The individual FP fits are shown in Figure 5, where the fixed parameters of the galaxy distribution used to fit the FP shift are given at the top of the plot. Each panel corresponds to a cluster, labelled by its CAN; the 29 clusters used to derive the parameters of the galaxy distribution are indicated by bold labels. The area of each point is proportional to the selection weight of the galaxy; the corresponding GINs are given at left. The solid line is the major axis of the global fit to the FP, and the cross on this line the centre of the global galaxy distribution, $(\overline{\log\sigma}, \overline{\log R_e}{-}b\overline{\langle SB_e\rangle})$. The dotted lines and ellipse are the major and minor axes and the 3σ contour of the cluster's FP, vertically offset from the global FP by the cluster's FP shift. The cluster's mean redshift cz, distance D, and peculiar velocity $V_{\rm pec}$, each with its estimated error, are given at the bottom of the panel. The distances and peculiar velocities are corrected for the residual selection bias discussed above.

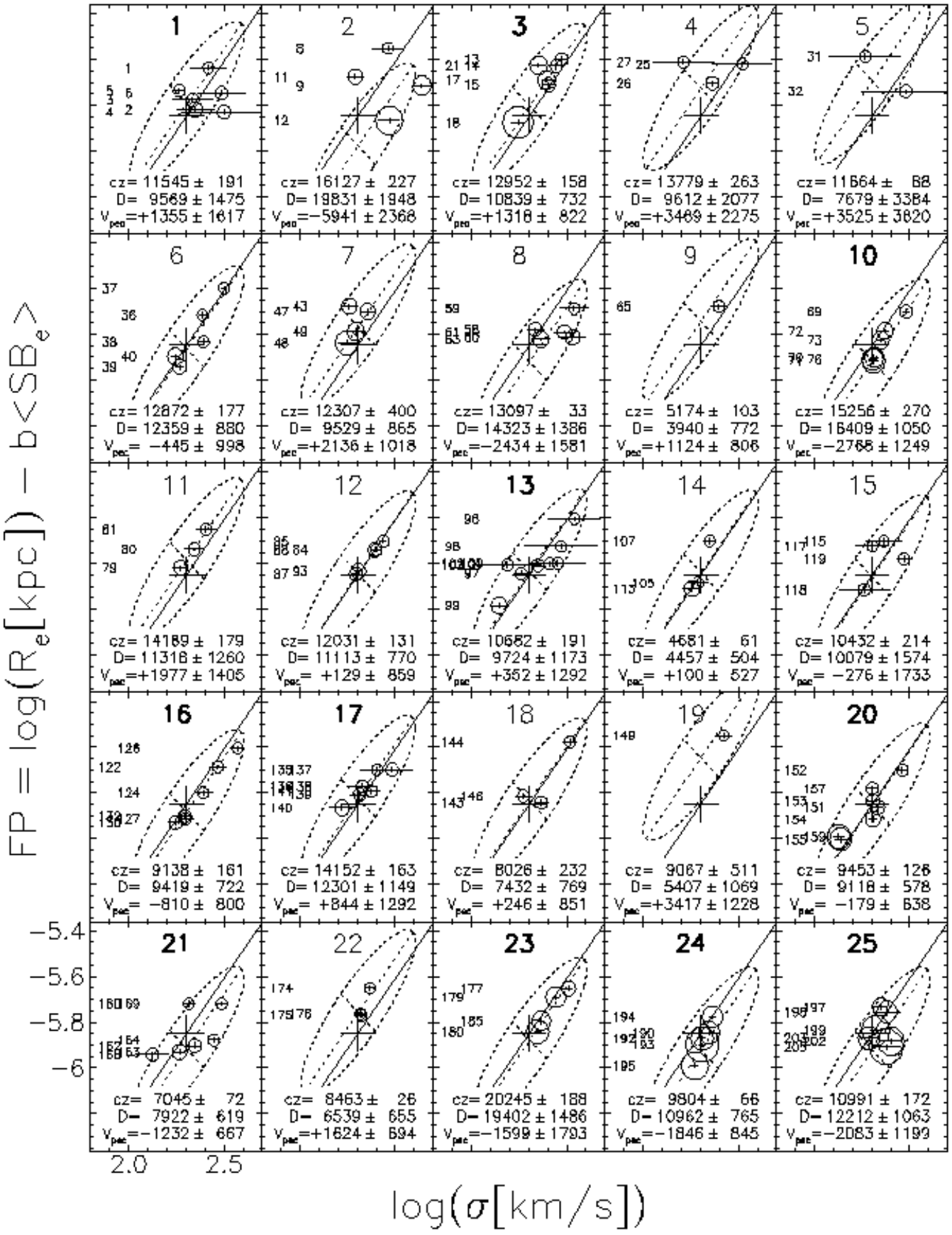

Figure 5. The FP distributions for each individual cluster. See text for description.

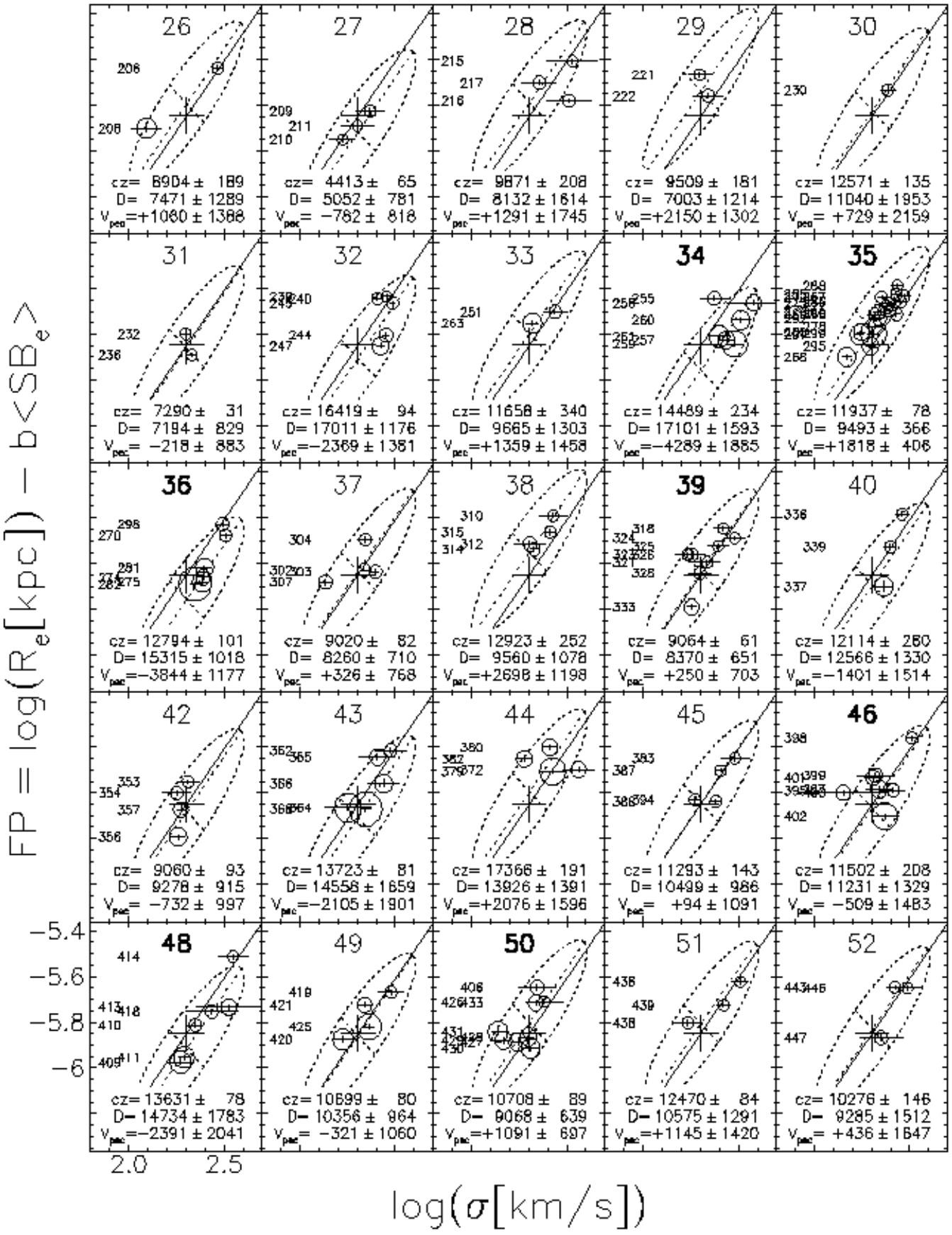

Figure 5. Continued.

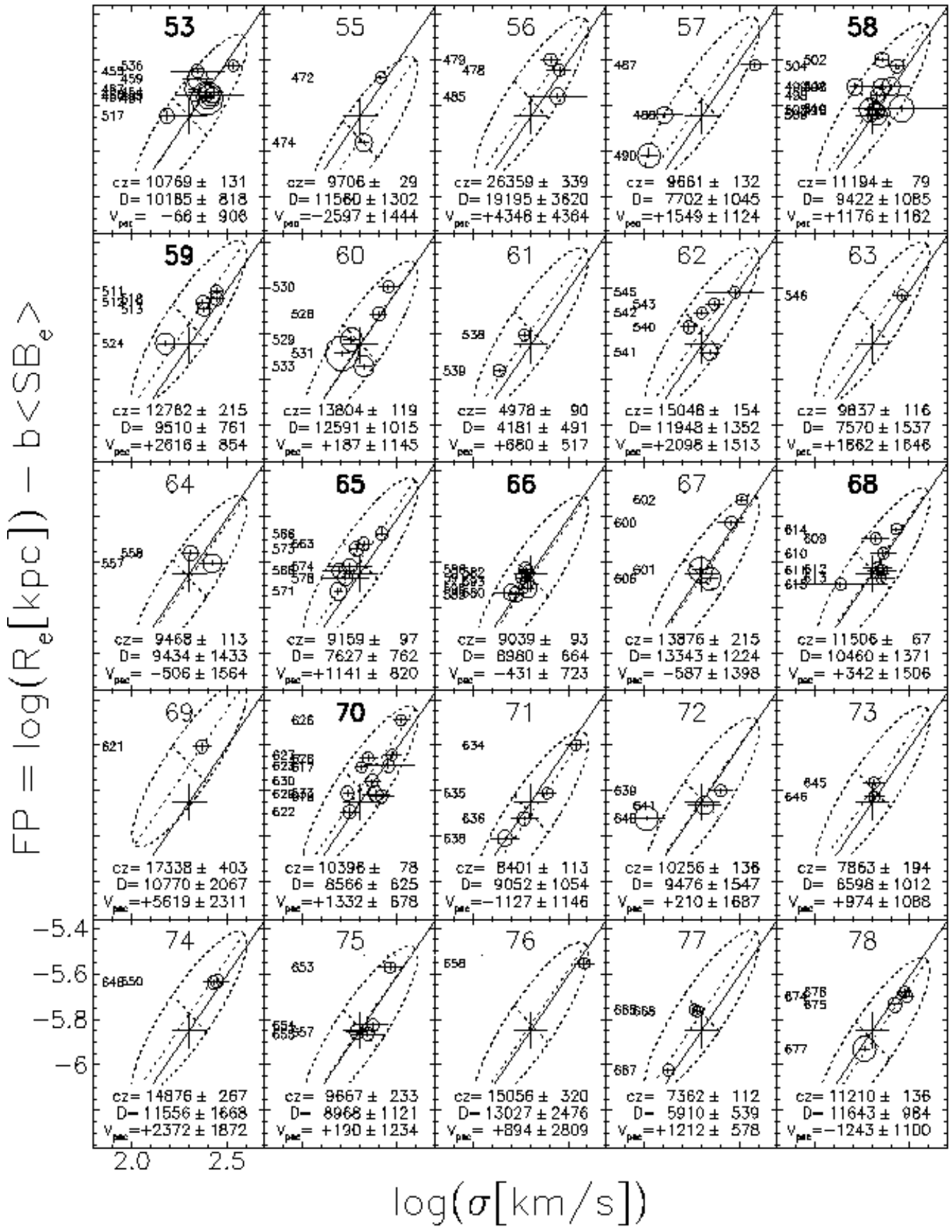

Figure 5. Continued.

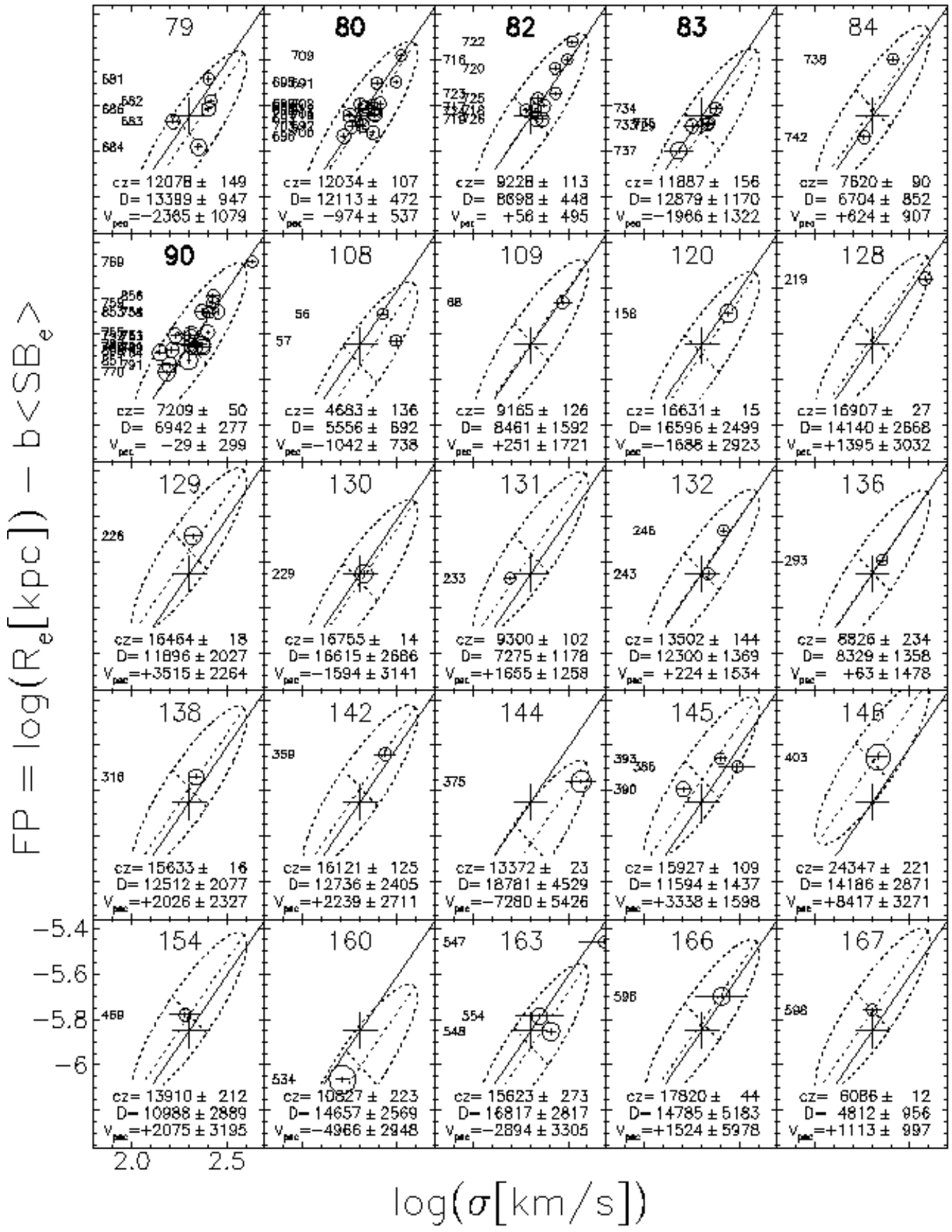

Figure 5. Continued.

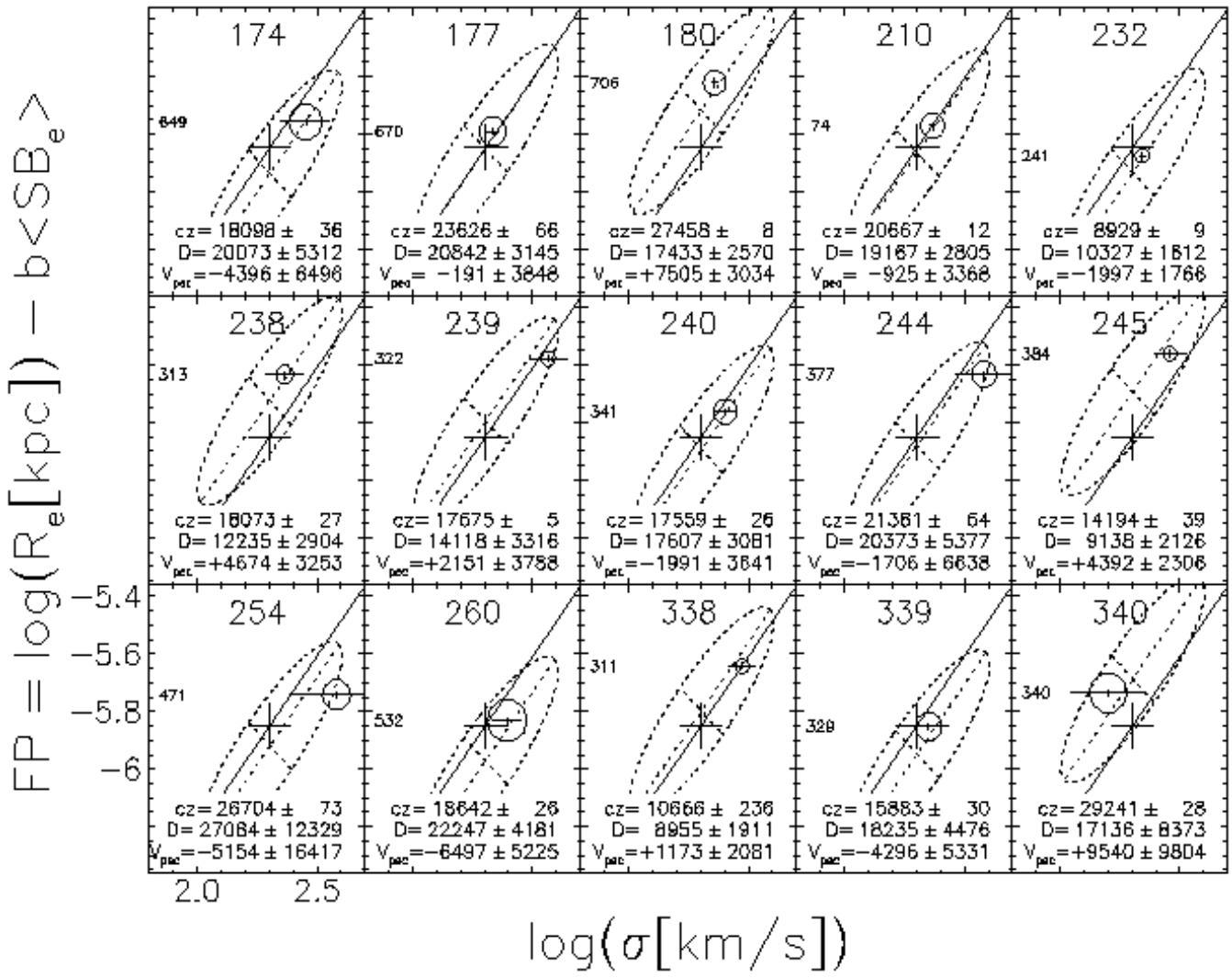

Figure 5. Continued.

The results are summarised in Table 7, which for each cluster gives: CAN, cluster name (in parentheses for fore- and background groups), number of galaxies used in the distance determination, Galactic longitude and latitude, the bias-corrected FP shift δ and its uncertainty, the bias correction ϵ_δ that was subtracted from the raw value of δ, the cluster redshift cz and its uncertainty Δcz, and the bias-corrected values of the cluster distance D and its uncertainty ΔD, the redshift cz_D corresponding to D, and the peculiar velocity V and its uncertainty ΔV. Note that some clusters are missing from this list: CAN 81 because it has been combined with CAN 80 (see Paper II); CANs 41, 47, 54 and a number of the fore- and background groups (CANs > 100) because no cluster members meet the selection criteria.

5.4 Tests and comparisons

Gibbons et al. (2000) have suggested that the large peculiar velocities found for some clusters are due to poor FP fits. For a heterogeneous sample of 20 clusters drawn from their own observations and the literature, they find that nearly half are poorly-fit by a FP and have twice the rms scatter of the well-fit clusters. The half of their clusters that have good FP fits all have peculiar velocities that are consistent with them being at rest in the CMB frame; the poorly-fit clusters show a much larger range of peculiar velocities. Gibbons et al. suggest that the large peculiar velocities detected for some clusters may result from those clusters being poorly fit (for whatever reason) by the global FP. The origin of the poor fits is not known, but the possibilities include intrinsic FP variations between clusters, failure to identify and remove interlopers, observational errors, the heterogeneity of the data, and combinations of these effects.

We therefore need to test whether some of the peculiar velocities we derive from the EFAR dataset are due to poor fits to the FP rather than genuine peculiar velocities. Figure 6 shows the peculiar velocities of the EFAR clusters as a function of the goodness-of-fit of their best-fit FP (as measured by the reduced χ^2 statistic). As noted above, even after removing outliers, there are still three clusters with very poor FP fits ($\chi^2/\nu > 3$; in fact CAN 2=A85 actually has $\chi^2/\nu = 11$, but is plotted at $\chi^2/\nu = 5$ for convenience). All three of these clusters have large negative peculiar veloc-

Table 7. Redshifts, distances and peculiar velocities for the EFAR clusters in the CMB frame

CAN	Name	N_g	l	b	δ	$\Delta\delta$	ϵ_δ	cz	Δcz	D	ΔD	cz_D	Δcz_D	V	ΔV
1*	A76	6	117.57	−56.02	−0.0528	0.0697	−0.0182	11545	191	9569	1475	10143	1658	+1355	1617
2	A85	4	115.23	−72.04	+0.1297	0.0466	−0.0310	16127	227	19831	1948	22514	2522	−5941	2368
3*	A119	6	125.80	−64.07	−0.0452	0.0309	−0.0204	12952	158	10839	732	11582	837	+1318	822
4	J3	3	125.87	−35.86	−0.1222	0.0953	−0.0103	13779	263	9612	2077	10192	2336	+3469	2275
5	J4	2	125.72	−49.85	−0.1525	0.1902	−0.0142	11664	88	7679	3384	8043	3713	+3525	3620
6*	A147	5	132.02	−60.34	+0.0143	0.0311	−0.0021	12872	177	12359	880	13337	1027	−445	998
7*	A160	4	130.33	−46.82	−0.0805	0.0416	−0.0218	12307	400	9529	865	10098	972	+2136	1018
8*	A168	5	134.36	−61.61	+0.0714	0.0432	−0.0107	13097	33	14323	1386	15658	1661	−2434	1581
9	A189	1	140.13	−59.99	−0.1053	0.0832	+0.0069	5174	103	3940	772	4034	810	+1124	806
10	J30	6	151.84	−75.04	+0.0694	0.0282	−0.0052	15256	270	16409	1050	18192	1295	−2768	1249
11*	A193	3	136.94	−53.26	−0.0630	0.0492	−0.0073	14189	179	11318	1260	12131	1450	+1977	1405
12*	J32	5	156.21	−69.05	−0.0045	0.0302	−0.0024	12031	131	11113	770	11896	884	+129	859
13*	A260	8	137.00	−28.17	−0.0142	0.0524	−0.0011	10682	191	9724	1173	10317	1322	+352	1292
14*	A262	3	136.59	−25.09	−0.0095	0.0486	+0.0033	4681	61	4457	504	4578	532	+100	527
15*	J7	4	143.10	−22.18	+0.0111	0.0673	+0.0007	10432	214	10079	1574	10718	1782	−276	1733
16*	J8	6	150.69	−34.33	+0.0360	0.0331	+0.0019	9138	161	9419	722	9975	811	−810	800
17*	A376	7	147.11	−20.52	−0.0258	0.0413	−0.0074	14152	163	12301	1149	13270	1339	+844	1292
18*	J9	3	143.01	−11.22	−0.0133	0.0449	−0.0001	8026	232	7432	769	7773	842	+246	851
19	J33	1	195.20	−58.30	−0.2018	0.0851	+0.0009	9067	511	5407	1069	5586	1141	+3417	1228
20*	A397	7	161.84	−37.33	+0.0080	0.0276	−0.0005	9453	126	9118	578	9638	647	−179	638
21*	A400	6	170.28	−45.00	+0.0687	0.0338	+0.0014	7045	72	7922	619	8311	682	−1232	667
22*	J28	3	183.86	−50.08	−0.0908	0.0433	+0.0008	8463	26	6539	655	6802	709	+1624	694
23	A419	4	214.31	−59.00	+0.0313	0.0340	−0.0077	20245	188	19402	1486	21962	1912	−1599	1793
24*	A496	5	209.59	−36.49	+0.0730	0.0306	−0.0044	9804	66	10962	765	11722	876	−1846	845
25*	J34	6	213.90	−34.95	+0.0732	0.0390	−0.0127	10991	172	12212	1063	13166	1238	−2083	1199
26	J10	2	197.18	−25.49	−0.0539	0.0758	−0.0073	8904	189	7471	1289	7815	1411	+1060	1388
27*	P597-1	3	198.62	−24.50	+0.0699	0.0657	+0.0070	4413	65	5052	781	5208	830	−782	818
28*	J35	3	217.47	−33.61	−0.0595	0.0869	−0.0066	9871	208	8132	1614	8543	1782	+1291	1745
29	J34/35	2	216.40	−34.19	−0.1091	0.0761	−0.0070	9509	181	7003	1214	7305	1321	+2150	1302
30	P777-1	1	218.49	−32.70	−0.0251	0.0789	−0.0135	12571	135	11040	1953	11812	2238	+729	2159
31	P777-2	2	220.77	−32.62	+0.0125	0.0493	+0.0052	7290	31	7194	829	7513	905	−218	883
32	P777-3	5	219.72	−31.71	+0.0560	0.0306	−0.0071	16419	94	17011	1176	18938	1463	−2369	1381
33	A533-1	2	224.95	−33.54	−0.0524	0.0600	−0.0114	11658	340	9665	1303	10251	1467	+1359	1458
34	A533	6	223.18	−33.65	+0.1079	0.0430	−0.0219	14489	234	17101	1593	19050	1984	−4289	1885
35	A548-1	18	230.28	−24.43	−0.0698	0.0170	−0.0059	11937	78	9493	366	10057	412	+1818	406
36	A548-2	6	230.40	−25.97	+0.1099	0.0300	−0.0146	12794	101	15315	1018	16854	1237	−3844	1177
37*	J11	4	118.21	+63.43	−0.0157	0.0375	−0.0018	9020	82	8260	710	8683	785	+326	768
38*	J12	4	50.52	+78.23	−0.0988	0.0495	−0.0054	12923	252	9560	1078	10132	1212	+2698	1198
39*	J13	8	28.27	+75.54	−0.0119	0.0337	+0.0004	9064	61	8370	651	8805	721	+250	703
40*	J36	3	332.77	+49.31	+0.0461	0.0465	−0.0054	12114	280	12566	1330	13578	1556	−1401	1514
42*	J14-1	4	8.80	+58.73	+0.0330	0.0432	−0.0039	9060	93	9278	915	9816	1025	−732	997
43	A1983	5	18.59	+59.60	+0.0597	0.0531	−0.0272	13723	81	14558	1659	15940	1994	−2105	1901
44	A1991	4	22.74	+60.52	−0.0530	0.0487	−0.0438	17366	191	13926	1391	15184	1658	+2076	1596
45*	J16	4	6.81	+48.20	−0.0035	0.0407	+0.0004	11293	143	10499	986	11195	1122	+94	1091
46*	J16W	7	5.08	+49.63	+0.0183	0.0524	−0.0089	11502	208	11231	1329	12032	1527	−509	1483
48	A2040	6	9.08	+51.15	+0.0676	0.0534	−0.0070	13631	78	14734	1783	16151	2148	−2391	2041
49*	A2052	4	9.42	+50.11	+0.0125	0.0420	−0.0160	10699	80	10356	964	11032	1095	−321	1060
50*	A2063	8	12.80	+49.70	−0.0455	0.0308	−0.0033	10708	89	9068	639	9581	714	+1091	697
51*	A2107	3	34.41	+51.51	−0.0406	0.0532	−0.0031	12470	84	10575	1291	11281	1471	+1145	1420
52*	J17	3	66.25	+49.99	−0.0184	0.0715	−0.0067	10276	146	9285	1512	9824	1694	+436	1647
53*	A2147	10	28.91	+44.53	+0.0026	0.0382	−0.0357	10769	131	10185	818	10838	927	−66	906
55	P386-2	2	40.53	+45.09	+0.1002	0.0491	−0.0024	9706	29	11560	1302	12410	1503	−2597	1444
56	A2148	3	41.97	+47.23	−0.0736	0.0887	−0.0316	26359	339	19195	3620	21696	4643	+4348	4364
57*	J18	3	39.95	+46.50	−0.0743	0.0591	−0.0032	9661	132	7702	1045	8069	1147	+1549	1124
58*	A2151	10	31.47	+44.64	−0.0469	0.0520	−0.0165	11194	79	9422	1085	9978	1218	+1176	1182
59*	J19	5	29.06	+43.50	−0.0966	0.0351	−0.0047	12782	215	9510	761	10077	855	+2616	854
60*	P445-1	5	31.19	+46.17	−0.0057	0.0374	−0.0251	13804	119	12591	1015	13607	1188	+187	1145
61	P445-2	2	28.77	+45.63	−0.0632	0.0499	+0.0083	4978	90	4181	491	4288	517	+680	517

Table 7. *Continued.*

CAN	Name	N_g	l	b	δ	$\Delta\delta$	ϵ_δ	cz	Δcz	D	ΔD	cz_D	Δcz_D	V	ΔV
62	A2162-N	5	50.36	+46.10	−0.0629	0.0499	−0.0066	15048	154	11948	1352	12859	1569	+2098	1513
63	A2162-S	1	48.36	+46.03	−0.0892	0.0872	+0.0010	9837	116	7570	1537	7925	1685	+1862	1646
64	J20	2	56.54	+45.58	+0.0221	0.0710	−0.0309	9468	113	9434	1433	9991	1608	−506	1564
65*	A2197	7	64.68	+43.50	−0.0566	0.0435	−0.0015	9159	97	7627	762	7987	836	+1141	820
66*	A2199	7	62.92	+43.70	+0.0198	0.0320	+0.0001	9039	93	8980	664	9483	741	−431	723
67*	J21	4	77.51	+41.64	+0.0174	0.0419	−0.0198	13876	215	13343	1224	14492	1447	−587	1398
68*	A2247	7	114.45	+31.01	−0.0127	0.0576	−0.0060	11506	67	10460	1371	11150	1560	+342	1506
69	P332-1	1	49.95	+35.22	−0.1640	0.0874	−0.0217	17338	403	10770	2067	11503	2361	+5619	2311
70*	J22	10	49.02	+35.93	−0.0581	0.0319	−0.0026	10396	78	8566	625	9023	694	+1332	678
71*	J23	4	85.81	+35.40	+0.0535	0.0501	+0.0025	8401	113	9052	1054	9564	1177	−1127	1146
72*	J24	3	69.51	+32.08	−0.0088	0.0722	−0.0096	10256	136	9476	1547	10038	1737	+210	1687
73	J25	2	91.82	+30.22	−0.0565	0.0661	+0.0013	7863	194	6598	1012	6865	1096	+974	1088
74	J26	2	69.59	+26.60	−0.0728	0.0680	−0.0329	14876	267	11556	1668	12405	1925	+2372	1872
75*	J27	4	80.41	+23.15	−0.0084	0.0541	+0.0001	9667	233	8968	1121	9470	1251	+190	1234
76	J38	1	36.09	−44.90	−0.0256	0.0887	−0.0306	15056	320	13027	2476	14119	2914	+894	2809
77*	P522-1	3	81.75	−41.26	−0.0770	0.0393	+0.0026	7362	112	5910	539	6124	579	+1212	578
78*	A2572	4	94.28	−38.95	+0.0444	0.0374	−0.0075	11210	136	11643	984	12505	1137	−1243	1100
79	A2589	5	94.64	−41.23	+0.0751	0.0309	−0.0022	12078	149	13399	947	14558	1121	−2365	1079
80*	A2593-N	16	93.44	−43.19	+0.0328	0.0170	−0.0016	12034	107	12113	472	13051	549	−974	537
82*	A2634	10	103.50	−33.08	−0.0026	0.0225	−0.0021	9228	113	8698	448	9169	498	+56	495
83*	A2657	5	96.73	−50.25	+0.0644	0.0396	−0.0024	11887	156	12879	1170	13945	1375	−1966	1322
84	A2666	2	106.71	−33.80	−0.0365	0.0545	+0.0035	7620	90	6704	852	6981	924	+624	907
90*	COMA	19	58.00	+88.00	+0.0017	0.0173	+0.0018	7209	50	6942	277	7238	302	−29	299
108	(A168)	2	134.36	−61.61	+0.0861	0.0532	+0.0055	4683	136	5556	692	5745	740	−1042	738
109	(A189)	1	140.13	−59.99	−0.0118	0.0851	−0.0191	9165	126	8461	1592	8906	1765	+251	1721
120	(A397)	1	161.84	−37.33	+0.0402	0.0709	−0.0314	16631	15	16596	2499	18423	3089	−1688	2923
128	(J35)	1	217.47	−33.61	−0.0359	0.0812	+0.0000	16907	27	14140	2668	15439	3188	+1395	3032
129	(J34/35)	1	216.40	−34.19	−0.1005	0.0830	−0.0466	16464	18	11896	2027	12798	2350	+3515	2264
130	(P777-1)	1	218.49	−32.70	+0.0377	0.0746	−0.0240	16755	14	16615	2686	18447	3322	−1594	3141
131	(P777-2)	1	220.77	−32.62	−0.0834	0.0698	+0.0007	9300	102	7275	1178	7602	1286	+1655	1258
132	(P777-3)	2	219.72	−31.71	−0.0070	0.0482	+0.0000	13502	144	12300	1369	13268	1596	+224	1534
136	(A548-2)	1	230.40	−25.97	−0.0031	0.0706	−0.0011	8826	234	8329	1358	8760	1503	+63	1478
138	(J12)	1	50.52	+78.23	−0.0580	0.0740	−0.0124	15633	16	12512	2077	13515	2428	+2026	2327
142	(J14-1)	1	8.80	+58.73	−0.0625	0.0936	−0.0490	16121	125	12736	2405	13778	2819	+2239	2711
144	(A1991)	1	22.74	+60.52	+0.1807	0.1143	−0.0374	13372	23	18781	4529	21166	5774	−7280	5426
145	(J16)	3	6.81	+48.20	−0.0985	0.0553	−0.0119	15927	109	11594	1437	12449	1659	+3338	1598
146	(J16W)	1	5.08	+49.63	−0.1752	0.0870	+0.0000	24347	221	14186	2871	15494	3433	+8417	3271
154	(P386-1)	1	37.09	+47.81	−0.0679	0.1159	−0.0129	13910	212	10988	2889	11752	3309	+2075	3195
160	(P445-1)	1	31.19	+46.17	+0.1585	0.0783	−0.0134	10827	223	14657	2569	16059	3092	−4966	2948
163	(A2162-S)	3	48.36	+46.03	+0.0706	0.0750	−0.0138	15623	273	16817	2817	18697	3493	−2894	3305
166	(A2199)	1	62.92	+43.70	−0.0371	0.1774	−0.0719	17820	44	14785	5183	16213	6248	+1524	5978
167	(J21)	1	77.51	+41.64	−0.0867	0.0852	+0.0025	6086	12	4812	956	4953	1013	+1113	997
174	(J26)	1	69.59	+26.60	+0.0896	0.1401	−0.0788	18098	36	20073	5312	22828	6899	−4396	6496
177	(P522-1)	1	81.75	−41.26	+0.0033	0.0710	−0.0300	23626	66	20842	3145	23832	4130	−191	3848
180	(A2593-N)	1	93.44	−43.19	−0.1306	0.0696	−0.0324	27458	8	17433	2570	19464	3215	+7505	3034
210	(J30)	1	151.84	−75.04	+0.0180	0.0676	−0.0234	20667	12	19167	2805	21659	3596	−925	3368
232	(P777-3)	1	219.72	−31.71	+0.0855	0.0673	+0.0009	8929	9	10327	1612	10999	1831	−1997	1766
238	(J12)	1	50.52	+78.23	−0.1249	0.1134	−0.0422	18073	27	12235	2904	13192	3382	+4674	3253
239	(J13)	1	28.27	+75.54	−0.0540	0.1141	−0.0477	17675	5	14118	3316	15412	3961	+2151	3788
240	(J36)	1	332.77	+49.31	+0.0445	0.0816	−0.0284	17559	26	17607	3081	19681	3863	−1991	3641
244	(A1991)	1	22.74	+60.52	+0.0315	0.1564	−0.1206	21381	64	20373	5377	23219	7014	−1706	6638
245	(J16)	1	6.81	+48.20	−0.1560	0.1049	−0.0198	14194	39	9138	2126	9660	2377	+4392	2306
254	(P386-1)	1	37.09	+47.81	+0.0711	0.2459	−0.1072	26704	73	27084	12329	32415	17745	−5154	16417
260	(P445-1)	1	31.19	+46.17	+0.1227	0.0970	−0.0630	18642	26	22247	4181	25696	5604	−6497	5225
338	(J12)	1	50.52	+78.23	−0.0493	0.0933	−0.0066	10666	236	8955	1911	9455	2132	+1173	2081
339	(J13)	1	28.27	+75.54	+0.0993	0.1160	−0.0367	15883	30	18235	4476	20472	5662	−4296	5331
340	(J36)	1	332.77	+49.31	−0.1612	0.1989	+0.0000	29241	28	17136	8373	19093	10428	+9540	9804

Note: clusters in the Fundamental Plane sample (Table 3) have their CANs in bold; clusters in the peculiar velocity sample are marked with an asterisk.

This table is also available as J/MNRAS/*vol*/*page* from NASA's Astrophysical Data Centre (ADC, http://adc.gsfc.nasa.gov) and from the Centre de Données astronomiques de Strasbourg (CDS, http://cdsweb.u-strasbg.fr).

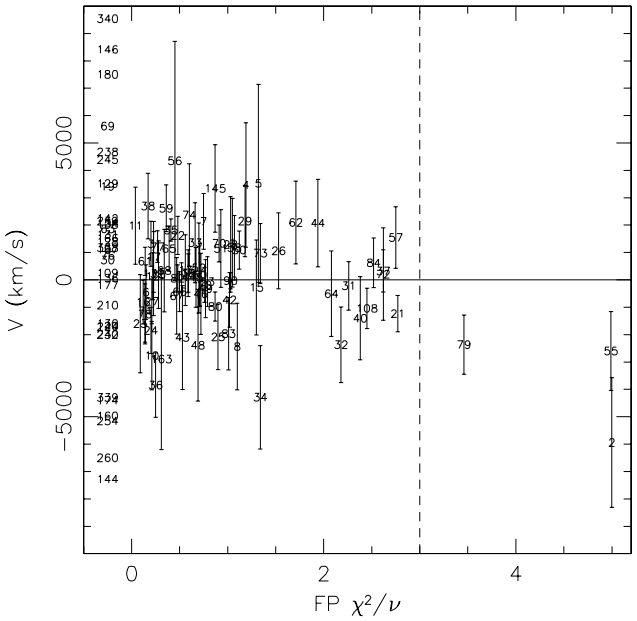

Figure 6. Cluster peculiar velocities as a function of the goodness-of-fit of their best-fit FP. Clusters indicated by their CANs; those with only single members have no χ^2/ν and are plotted at the left of the figure to show their peculiar velocities.

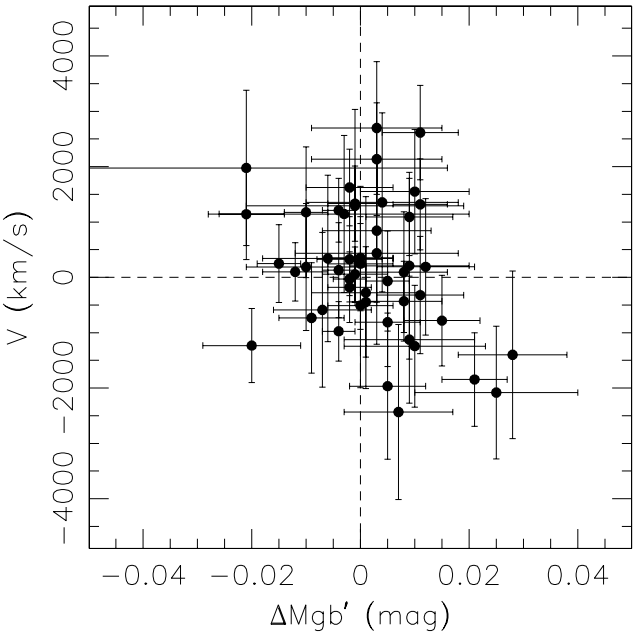

Figure 7. The distribution of cluster peculiar velocities with respect to the cluster offsets from the global Mg–σ relation of Paper V.

ities, detected at nominal significance levels of 1.8–2.5σ. The poor quality of the FP fits raises considerable doubts about the reality of the peculiar velocity estimates, however, and we therefore omit these clusters from all subsequent analysis. The remaining clusters generally have acceptable fits ($\chi^2/\nu\approx1$). There are 10 clusters with χ^2/ν=2–3, but none of these have significant peculiar velocities (the strongest detection is at the 1.8σ level). Apart from the three clusters with χ^2/ν>3, the clusters are all adequately fitted by the global FP, and there is no evidence for any increased scatter in the peculiar velocities for poorer FP fits.

Another possible source of systematic errors are the small biases in the recovered parameters of the best-fitting FP (see §4 above). If we apply the corrections for these biases derived from our simulations (Figure 2) and re-derive the peculiar velocities with this bias-corrected FP, we find that the peculiar velocities of the clusters are not significantly altered: the peculiar velocity of Coma changes by $+14\,\mathrm{km\,s^{-1}}$, and the rms difference in peculiar velocity between our standard solution and the bias-corrected solution is only $67\,\mathrm{km\,s^{-1}}$.

We can also attempt to test whether differences in the mean stellar populations between clusters produce spurious peculiar velocities, by looking for a correlation between the peculiar velocities and the offset of each cluster from the global Mg–σ relation derived in Paper V. The correlation coefficient for the distribution (shown in Figure 7) is −0.30, but 1000 simulations of the observed distribution show that, allowing for the estimated errors, this value does not indicate a correlation significant at the 95% level. However, while there is no positive evidence that stellar population differences are leading to spurious peculiar velocities, this test cannot rule out this possibility. Figure 10 of Paper V shows that the joint distribution of residuals about the FP and Mg–σ relations is consistent with simple stellar population models if one invokes sufficiently large (and possibly correlated) scatter in the ages and metallicities of the galaxies. Against this possibility we can set the generally good agreement between the distance estimates obtained from the FP and other methods (such as the Tully-Fisher relation and surface brightness fluctuations) which have different dependences on the stellar populations.

Finally, we can perform a direct comparison between the peculiar velocities we measure and those obtained by other groups for the same clusters. Figure 8 shows comparisons with the Tully-Fisher estimates of Giovanelli et al. (1998b; SCI) and Dale et al. (1999b; SCII), and the FP estimates of Hudson et al. (1997; SMAC) and Gibbons et al. (2000; GFB). The flattening in the $V_{\rm EFAR}$–$V_{\rm other}$ distributions is due to the fact that the uncertainties in the EFAR peculiar velocities are generally larger than those of the other measurements—although the error per galaxy is similar in all cases, the EFAR sample typically has a smaller number of galaxies per cluster. A χ^2-test shows that the peculiar velocity measurements are consistent within the errors in all three comparisons.

6 BULK MOTIONS

6.1 Cluster sample

In analysing the peculiar motions of the clusters in the EFAR sample we confine ourselves to the subsample of clusters with 3 or more galaxies ($N_g\geq3$), $cz\leq15000\,\mathrm{km\,s^{-1}}$ and $\delta V\leq1800\,\mathrm{km\,s^{-1}}$. These criteria are illustrated in Figure 9, and are chosen because: (i) they eliminate all the fore- and background clusters, for which the selection functions have not been directly measured and are only poorly approximated by the selection function of the main cluster onto which they are projected; (ii) they eliminate the

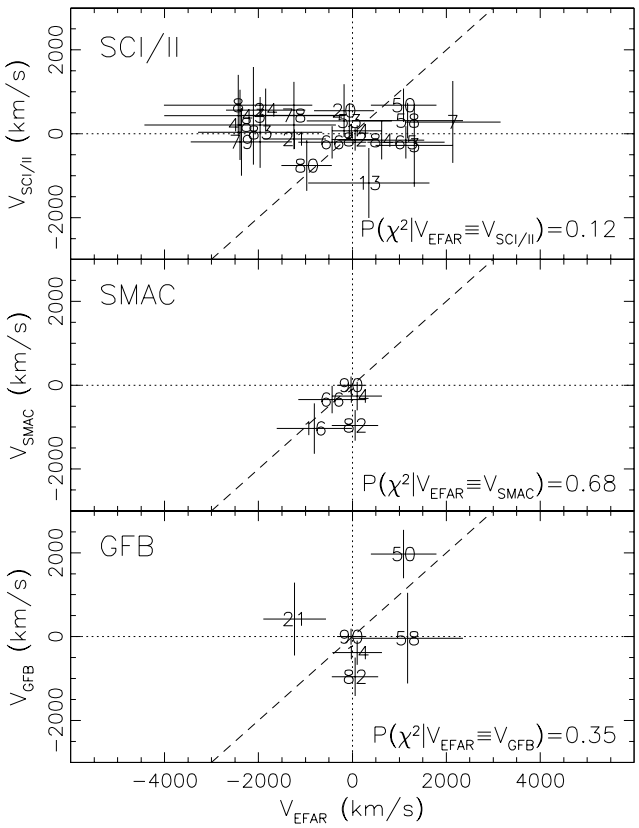

Figure 8. Comparisons of EFAR peculiar velocities of clusters in common with SCI/II (Giovanelli et al. 1998b, Dale et al. 1999b), SMAC (Hudson et al. 1997) and GFB (Gibbons et al. 2000).

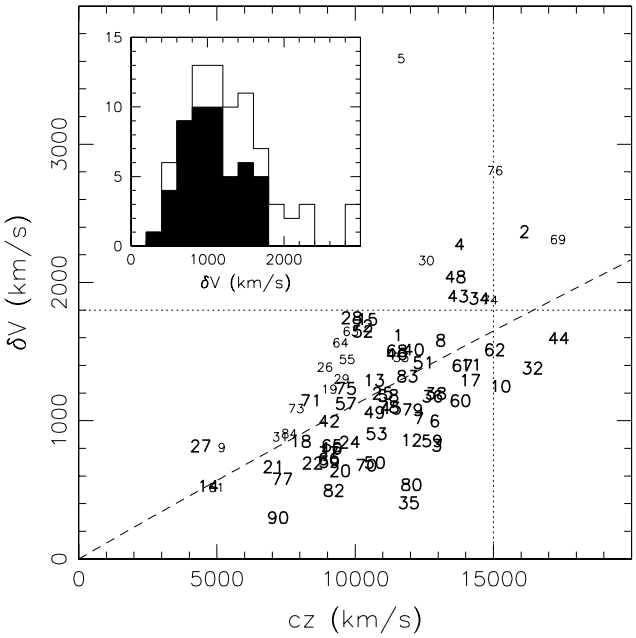

Figure 9. The selection of clusters for the peculiar velocity analysis. The cluster's peculiar velocity errors are plotted as a function of their redshifts. Each cluster is marked by its CAN, with clusters having 3 or more galaxies in a larger font; fore- and background groups (CAN>100) are not shown. The selection limits in cz and δV are indicated by the dotted lines. The distribution of peculiar velocity errors is shown in the inset: the open histogram is for all clusters, the filled histogram for the selected clusters.

clusters with only 1 or 2 galaxies in the FP fit, where it is not possible to check if galaxies are cluster interlopers or FP outliers; (iii) they eliminate the higher-redshift clusters, which have proportionally higher uncertainties in their peculiar velocities (and in any case sample the volume beyond cz=15000 km s^{-1} too sparsely to be useful); (iv) they eliminate clusters with large uncertainties in their peculiar velocities, resulting from large measurement errors for individual galaxies exacerbated by a small number of galaxies in the cluster—restricting the subsample to $\delta V \leq 1800$ km s^{-1} (the peculiar velocity error for a cluster with a FP distance from 3 galaxies with a distance error per galaxy of 20%) represents a compromise between using clusters with better-determined peculiar velocities and keeping the largest possible cluster sample.

We also eliminate from the sample the three clusters which were identified in the previous section as having unacceptably poor FP fits (CAN 2=A85, CAN 55=P386-2 and CAN 79=A2589); two of these would be eliminated in any case: A85 because it has cz>15000 km s^{-1}, and P386-2 because it has only two galaxies. We also eliminate the two components of A548 (CAN 35=A548-1 and CAN 36=A548-2), since the substructure in this region (Zabludoff et al. 1993, Davis et al. 1995) makes cluster membership problematic and since the high relative velocity of the two main subclusters is not relevant to the large-scale motions we are investigating (Watkins 1997).

The subsample selected in this way for the analysis of the peculiar motions comprises 50 clusters (25 in HCB, 25 in PPC); they are indicated by an asterisk in Table 7. The distribution of the peculiar velocity uncertainties for this subsample is shown in the inset to Figure 9); the median peculiar velocity error is 1060 km s^{-1}. Figure 10 shows the projection of the sample on the sky in Galactic coordinates, with the amplitude of the clusters' peculiar velocities in the CMB frame indicated by the size of the symbols. Inflowing clusters (circles) and outflowing clusters (asterisks) are fairly evenly distributed over the survey regions. The median direction of the clusters belonging to the peculiar velocity sample in the HCB region is (l,b)=(42°,48°), and in the PPC region is (l,b)=(152°,-36°); the angle between these two directions is 128°.

6.2 Bulk motions

The peculiar velocities of the sample clusters as a function of redshift are shown in Figure 11. The mean peculiar velocity of the whole sample ($\langle V\rangle$=159±158 km s^{-1}) is consistent, within the errors, with no net inflow or outflow. This need not have been the case, as the FP zeropoint is based on the 29 clusters listed in Table 3, which make up only 26 of the 50 clusters in the peculiar velocity sample. The mean peculiar velocities of each of the two sample regions separately are also consistent with zero inflow or outflow: $\langle V_{\rm HCB}\rangle$=+383±229 km s^{-1}; $\langle V_{\rm PPC}\rangle$=−65±217 km s^{-1}. A χ^2 test shows that the observed peculiar velocities are consistent with strictly zero motions (i.e. no bulk or random motions at all) at the 2% level. If the one cluster with a 3σ pecu-

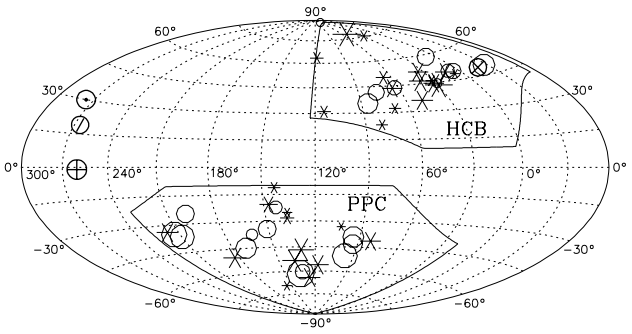

Figure 10. The projection on the sky in Galactic coordinates of the EFAR peculiar velocities in the CMB frame. Clusters with positive (negative) peculiar velocities are indicated by asterisks (circles); marker sizes are related to the amplitude of the peculiar velocity. Other markers show the directions with respect to the CMB frame of the Local Group dipole (⊙), the Lauer & Postman (1994) dipole (⊗), the SMAC (Hudson et al. 1999) dipole (⊕), and the LP10K (Willick 1999) dipole (⊘).

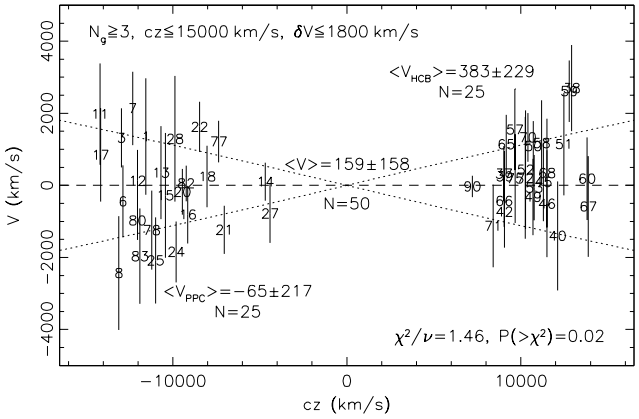

Figure 11. Peculiar velocities of the EFAR clusters as a function of redshift. The clusters in PPC are given negative redshifts, but in all cases positive peculiar velocities indicate outflow and negative peculiar velocities inflow. Both redshifts and peculiar velocities are in the CMB frame. Clusters are indicated by the CANs. Peculiar velocity errors are shown, but redshift errors (which are small) are omitted for clarity. The dotted curves correspond to the typical $\pm1\sigma$ peculiar velocity errors for clusters with peculiar velocities based on 3 galaxies. The unweighted mean peculiar velocity, and the number of sample clusters, are shown for the HCB and PPC regions separately and for the sample as a whole. The χ^2 probability that the observed peculiar velocities are consistent with strictly zero motions is also given.

liar velocity detection (J19, CAN=59) is omitted, this rises to 8%. If the peculiar velocity errors were under-estimated by 5% (10%), then the fit is consistent at the 6% (15%) level. If random thermal motions with an rms of 250 km s^{-1} (500 km s^{-1}) are assumed, then the fit is consistent at the 5% (30%) level. There is, therefore, no evidence in the EFAR sample for significant bulk motions in the HCB or PPC volumes.

The components in Supergalactic coordinates of the mean peculiar velocity in redshift shells are shown in Figure 12. There is no sign of any trend with redshift in the mean peculiar velocity, either for the whole sample or for

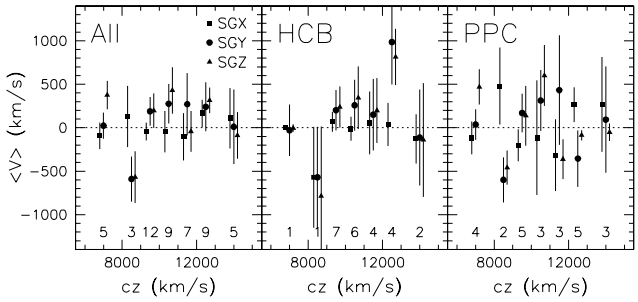

Figure 12. The mean peculiar velocity in radial shells. The clusters are grouped into 7 redshift ranges: the first is 4000–8000 km s^{-1}, the next five cover 8000 km s^{-1} to 13000 km s^{-1} in 1000 km s^{-1} steps, and the last is 13000–15000 km s^{-1}. The left panel shows the whole sample of 50 clusters, the middle panel shows the 25 HCB clusters, and the right panel shows the 25 PPC clusters. The Supergalactic X, Y and Z components are shown as filled squares, circles and triangles respectively (with small offsets in redshift for clarity). The number of clusters in each redshift range is indicated at the bottom of each panel.

the two regions separately. None of the components of the mean peculiar velocity are significant in any redshift bin apart from the 12000–13000 km s^{-1} bin in HCB, which is due to J19 (CAN=59)—cf. Figure 11.

We can estimate the intrinsic dispersion of the peculiar velocity field using the maximum likelihood approach described in Paper VI (see Section 2.1 and Appendix A; cf. Watkins 1997). The upper panels of Figure 13 show the distributions of peculiar velocities, both radially and in Supergalactic coordinates, for the HCB and PPC regions separately and for the whole sample. The peculiar velocities in all cases have means close to zero, and the question is how large an intrinsic dispersion is required, combined with the observational uncertainties, to reproduce the observed scatter in the peculiar velocities. The lower panels of Figure 13 show the relative likelihood, $\Delta \ln \mathcal{L} = \ln \mathcal{L}_{\max} - \ln \mathcal{L}$, as a function of the assumed intrinsic dispersion. The most likely estimate of the three-dimensional velocity dispersion for the whole sample is about 600 km s^{-1}, but the 1σ range is 0–1200 km s^{-1}. The most likely dispersions for the HCB and PPC regions separately are about 300 km s^{-1} and 700 km s^{-1} respectively. Hence the intrinsic dispersion of the clusters' peculiar velocities is not well-determined by this data, due to the large uncertainties in the observed peculiar velocities.

6.3 Comparisons with other results

A comparison of the EFAR bulk motion to other measurements of bulk motions on various scales, and to theoretical predictions, is given in Figure 14. The figure shows the reported bulk motions from a number of other observational studies as a function of the effective scale of the sample. Also shown is the theoretical prediction for the bulk motion measured with a top-hat window function of radius R (in h^{-1} Mpc) for a fairly 'standard' flat ΛCDM cosmology having a power spectrum with shape parameter Γ=0.25, normalisation σ_8=1.0 and Hubble constant h=0.7 (corresponding to Ω_0=0.36 and Ω_Λ=0.64; see, e.g., Coles & Lucchin 1995, p.399).

This comparison is limited by a number of factors:

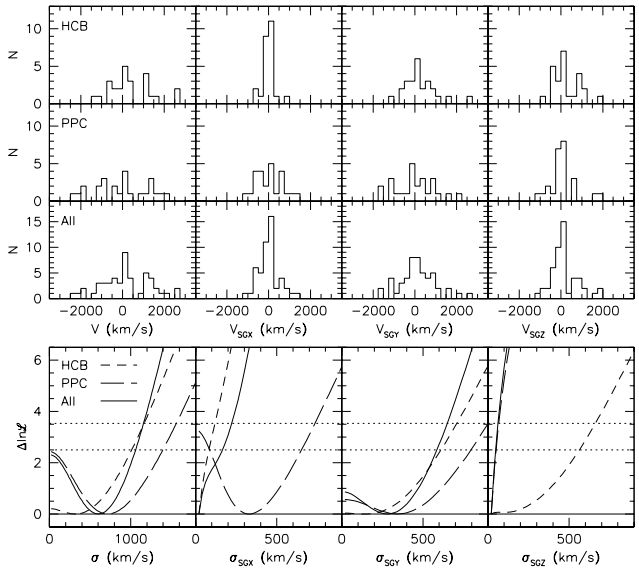

Figure 13. Upper panels: The histograms of the peculiar velocities for the HCB and PPC regions and the whole sample, both radially and projected in Supergalactic (X,Y,Z) coordinates. Lower panels: The relative likelihood, $\Delta \ln \mathcal{L} = \ln \mathcal{L}_{\max} - \ln \mathcal{L}$, as a function of the assumed intrinsic dispersion, both overall and in each Supergalactic coordinate. The solid curve is for the whole sample; the dashed and long-dashed curves are for the HCB and PPC regions respectively. The upper dotted line is the 1σ confidence level for the whole sample, while the lower dotted line is the 1σ confidence level for both individual regions.

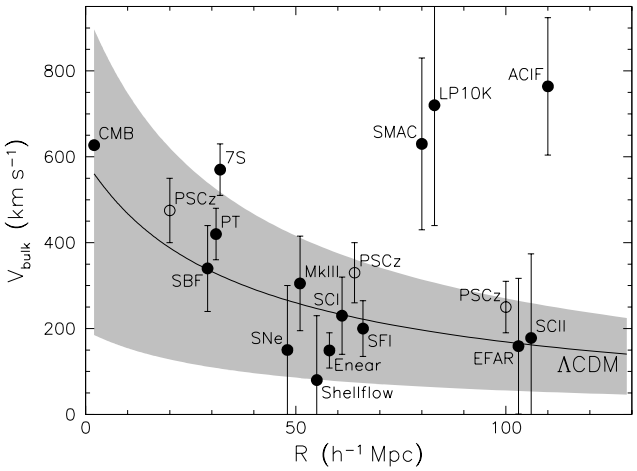

Figure 14. Bulk motion amplitude as a function of scale. The theoretical curve is the expectation for the bulk motion within a spherical volume of radius R in a ΛCDM model (Γ=0.25, σ_8=1.0, h=0.7); the grey region shows the 90% range of cosmic scatter. The bulk motions determined in various studies are shown at the 'effective scale' of each sample (which is generally only approximate). The bulk motions shown are for the Local Group w.r.t. the CMB (Kogut et al.1993), 7S (Lynden-Bell et al. 1988), ACIF (Lauer & Postman 1994; Colless 1995), SFI (Giovanelli et al. 1998a), SCI (Giovanelli et al. 1998b), SCII (Dale et al. 1999a), MkIII (Dekel et al. 1999), SMAC (Hudson et al. 1999), LP10K (Willick 1999), Shellflow (Courteau et al. 2000), SNe (Riess 2000), ENEAR (da Costa et al. 2000), SBF (Tonry et al. 2000), PT (Pierce & Tully 2000), and EFAR (this work). Also shown are the predicted bulk motions derived from the PSCz redshift survey (Saunders et al. 2000; Dekel 2000).

(i) The finite, sparse and non-uniform observed samples do not have top-hat window functions, and their effective scales R are not well-defined (compare this figure with the similar figure in Dekel (2000)); this uncertainty is ameliorated by the slow decrease in the expected bulk motion with scale. (ii) Only the amplitudes of the bulk motions are compared, and not the directions; however, the observed bulk motions that are significantly different from zero have a common direction to within about 30°, close to the direction of the CMB dipole. (iii) The uncertainties in the measured bulk motions are only crudely estimated in some studies, and ignore or under-estimate the systematic biases. Despite these limitations, the figure does show that, allowing for both observational uncertainties and cosmic variance, the measured bulk motions are in most cases quite consistent with the theoretical predictions (which vary relatively little for any model that is consistent with the currently-accepted ranges of the cosmological parameters). In this section and the next we determine the extent to which the EFAR results are consistent with the models and with the possibly-discrepant results of Lauer & Postman (1994; ACIF) and Hudson et al. (1999; SMAC). The bulk flow obtained by Willick (1999; LP10K) is similar to the SMAC result, and is not considered explicitly.

We can test whether the observed EFAR peculiar velocity field is consistent with the bulk motions claimed by other authors. The bulk motion of the Lauer & Postman (1994) cluster sample in the CMB frame, based on brightest cluster galaxy distances as re-analysed by Colless (1995), is $764\,\mathrm{km\,s^{-1}}$ in the direction $(l,b)=(341°,49°)$. This direction is only 39° from the median direction of the HCB clusters in the EFAR sample, and its antipole is just 15° from the median direction of the PPC clusters. Consequently the EFAR sample is able to provide a strong test of the existence of the Lauer & Postman bulk motion. Figure 15a shows the peculiar velocities of the EFAR sample as a function of the cosine of their angle with respect to the direction of the Lauer & Postman dipole. The best-fit bulk flow in the Lauer & Postman direction has $V=250\pm209\,\mathrm{km\,s^{-1}}$, and is consistent with zero at the 1.2σ level. A χ^2 test finds that a pure Lauer & Postman bulk motion of $764\,\mathrm{km\,s^{-1}}$ in this direction is consistent with the data at only the 0.2% level.

The bulk motion of the SMAC sample, for which peculiar velocities are derived from FP distances by Hudson et al. (1999), is $630\,\mathrm{km\,s^{-1}}$ in the direction $(l,b)=(260°,-1°)$. The median direction of the HCB clusters is 57° from the antipole of this motion, and the median direction of the PPC clusters is 76° from the antipole. Hence the EFAR sample is less well-suited to testing for bulk motions in this direction. Nonetheless, the formal rejection of the SMAC motion is even stronger than for the Lauer & Postman motion. Figure 15b shows the peculiar velocities of the EFAR sample as a function of the cosine of their angle with respect to the SMAC dipole. The best-fit bulk flow along the SMAC direction has $V=-536\pm330\,\mathrm{km\,s^{-1}}$ (i.e. in the opposite direction), and is consistent with zero bulk motion at the 1.6σ level. A χ^2 test finds that a pure SMAC bulk motion of $630\,\mathrm{km\,s^{-1}}$ in this direction is consistent with the data at only the 0.04% level.

It is worth noting that an observed bulk flow amplitude

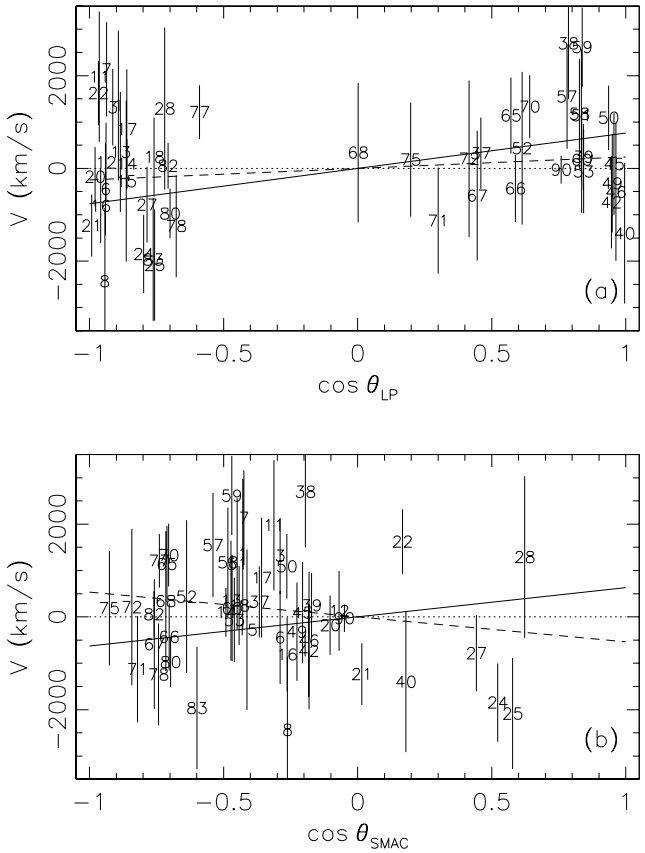

Figure 15. The peculiar velocities of the EFAR clusters versus the cosine of their angle with respect to the direction of (a) the Lauer & Postman dipole, (l,b)=(341°,49°), and (b) the SMAC dipole, (l,b)=(260°,−1°). Each cluster is indicated by its CAN. The solid line shows the claimed relation; the dotted line is the best fit to the EFAR data (see text for details).

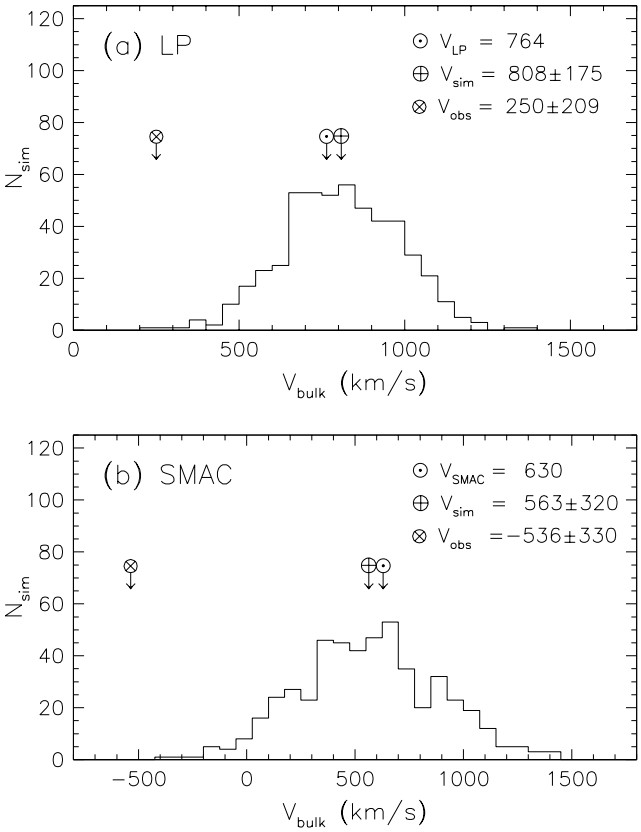

Figure 16. Simulations of the recovery from the EFAR dataset of (a) the Lauer & Postman (1994; LP) bulk flow and (b) the Hudson et al. (1999; SMAC) bulk flow. The histograms are the distributions of the recovered bulk flow amplitude in the directions of the LP and SMAC dipoles. The labelled arrows show the true amplitude ($V_{\rm LP}$ or $V_{\rm SMAC}$), the mean of the recovered amplitudes ($V_{\rm sim}$) and its rms scatter, and the observed amplitude ($V_{\rm obs}$) and its uncertainty.

of zero would be consistent with the Lauer & Postman flow at less than the 0.2% level, but consistent with the SMAC flow at the 3.2% level—if the real bulk flow is small, therefore, the apparently high significance of the rejection of the SMAC flow may be the result of the large uncertainty in the observed amplitude of the flow.

These χ^2 tests do not take into account the correlated errors in the peculiar velocity estimates. We therefore carry out Monte Carlo simulations of the EFAR dataset, including the effects of the correlated errors, in order to check the consistency of the observed peculiar velocities with the claimed bulk flows of Lauer & Postman (LP) and Hudson et al. (SMAC). Figure 16 shows the distributions of the bulk flow amplitudes recovered from 500 simulations of the LP and SMAC bulk motions. The mean values of the recovered bulk flow amplitude ($V_{\rm sim}$) are very close to the true values ($V_{\rm LP}$ or $V_{\rm SMAC}$), although in each case there is a small but statistically significant bias. However the value of the bulk flow amplitude derived from the actual EFAR dataset ($V_{\rm obs}$) is in both cases far out on the wing of the distribution: only one of the 500 simulations of the Lauer & Postman flow, and none of the 500 simulations of the SMAC flow, yields a bulk flow amplitude less than the observed value. Hence the observations are consistent with a pure Lauer & Postman bulk flow only at the 0.2% level, and with a pure SMAC bulk flow at less than the 0.2% level. The correlated errors in the peculiar velocities do not significantly alter the results obtained from the χ^2 tests.

6.4 Comparisons with theoretical models

The above comparisons assume pure bulk flows and ignore the greater complexity of the real velocity field. We can make more realistic comparisons if we adopt a more detailed model for the velocity field. In principle this approach also allows us to use the observed peculiar velocities to discriminate between different cosmological models. The velocity field models are characterised by a mass power spectrum, which determines the velocity field on large scales where the dynamics are linear, and a small-scale rms 'thermal' motion, σ_*, which approximates the effects of non-linear dynamics on small scales. Given such a model, the method for computing the expected bulk flow in a particular sample, and for estimating the probability of an observed bulk flow, has been developed by Kaiser (1988) and Feldman & Watkins (1994, 1998).

As shown by Feldman & Watkins (1994), the covariance matrix for the maximum likelihood estimator of the

bulk flow in a sample is given by the sum of a 'noise' term, which depends on the spatial distribution of the clusters, the errors in their peculiar velocities and the thermal rms motions, and a 'velocity' term, which also depends on the power spectrum of the assumed cosmological model. We adopt a thermal rms motion of σ_*=250 km s^{-1}. Although this value is not well-determined it has little effect on the results (as we show below), since it enters in quadrature sum with the uncertainties on the cluster peculiar velocities, which are generally much larger (see Table 7). Our adopted cosmological model has a CDM-like power spectrum with Γ=0.25 and σ_8=1.0, consistent with the power spectrum measured from the APM galaxy survey (Baugh & Efstathiou 1993) and the PSCz redshift survey (Sutherland et al. 1999). This corresponds to the currently-favoured flat ΛCDM cosmology with $H_0 \approx 70$ km s^{-1} Mpc^{-1}, $\Omega_0 \approx 0.35$ and $\Omega_\Lambda \approx 0.65$.

The survey's sensitivity to the power spectrum is determined by its window function. Figure 17a shows the window function for the EFAR sample along the Supergalactic X, Y and Z axes; the Y axis in particular shows the effect of correlated errors resulting from not having a full-sky sample. The model power spectrum is shown in Figure 17b. The product of the power spectrum and the window function, shown in Figure 17c, gives the relative contributions of different scales to the covariance in the measured bulk velocity. The bulk velocity depends on a broad range of scales, with the largest contributions coming from scales of a few hundred h^{-1} Mpc.

For the EFAR survey the 'noise' component of the covariance matrix (in Supergalactic coordinates) is

$$R^{\epsilon}_{ij} = \begin{bmatrix} +101655 & +47914 & -24001 \\ +47914 & +65373 & -39617 \\ -24001 & -39617 & +87567 \end{bmatrix} \quad (13)$$

while the 'velocity' component is

$$R^{v}_{ij} = \begin{bmatrix} +37169 & +17211 & -344 \\ +17211 & +23165 & -6084 \\ -344 & -6084 & +20980 \end{bmatrix} . \quad (14)$$

Thus the overall covariance matrix $\boldsymbol{R}$ is

$$R_{ij} = R^{\epsilon}_{ij} + R^{v}_{ij} = \begin{bmatrix} +138824 & +65125 & -24345 \\ +65125 & +88538 & -45701 \\ -24345 & -45701 & +108547 \end{bmatrix} . \quad (15)$$

It is immediately apparent that (for the model considered here) the covariance matrix is dominated by the 'noise' term.

The maximum likelihood estimate, $\boldsymbol{U}$, for the bulk flow of the sample clusters is given by

$$U_i = R^{\epsilon}_{ij} \sum_n \frac{\hat{r}_{n,j} v_n}{\sigma_n^2 + \sigma_*^2} \quad (16)$$

where U_i is the ith component of the bulk flow, R^{ϵ}_{ij} is the 'noise' covariance matrix, $\hat{r}_{n,j}$ is the jth component of the unit vector of the nth cluster, v_n and σ_n are the cluster's peculiar velocity and its uncertainty, and σ_* is the assumed rms thermal motion of the model. For the EFAR sample, the maximum likelihood bulk flow vector in Supergalactic coordinates is $(-24,\ -6,\ +717)$ km s^{-1}, almost entirely in the SGZ axis. In Galactic coordinates this is 718 km s^{-1} in the direction $(l,b)=(45.4^\circ,+5.9^\circ)$.

However this formal result is rather ill-determined, since it is far from the main axis of the EFAR sample (cf. Figure 10). An indication of the uncertainty can be obtained by ignoring the cross-correlations in the covariance matrix and estimating the rms error as $(\mathrm{Trace}(R^{\epsilon}))^{1/2}$=505 km s^{-1}. In the context of the assumed cosmological model, the probability of measuring a bulk flow vector $\boldsymbol{U}$ can be obtained by computing the χ^2 statistic from the covariance matrix as

$$\chi^2 = U_i R^{-1}_{ij} U_j \ . \quad (17)$$

The probability (given the cosmological model and the properties of the sample) of observing a bulk flow with a value of χ^2 greater than this is given by the appropriate integral over the χ^2 distribution with 3 degrees of freedom (the 3 components of $\boldsymbol{U}$). For the EFAR sample this procedure yields χ^2=6.1 with 3 degrees of freedom, and hence the observed bulk flow is consistent with the model at the 11% confidence level. If the rms thermal motion σ_* is set to be zero rather than 250 km s^{-1}, the observations are still consistent with the model at the 9% confidence level.

The expectation value for the bulk motion (given the cosmological model and the properties of the sample) can be obtained as

$$V = \frac{(\sigma_1\sigma_2\sigma_3)^{-1}}{(2\pi)^{3/2}} \int |V| \exp\left(-\sum_i \frac{V_i^2}{2\sigma_i^2} \right) d^3V \ , \quad (18)$$

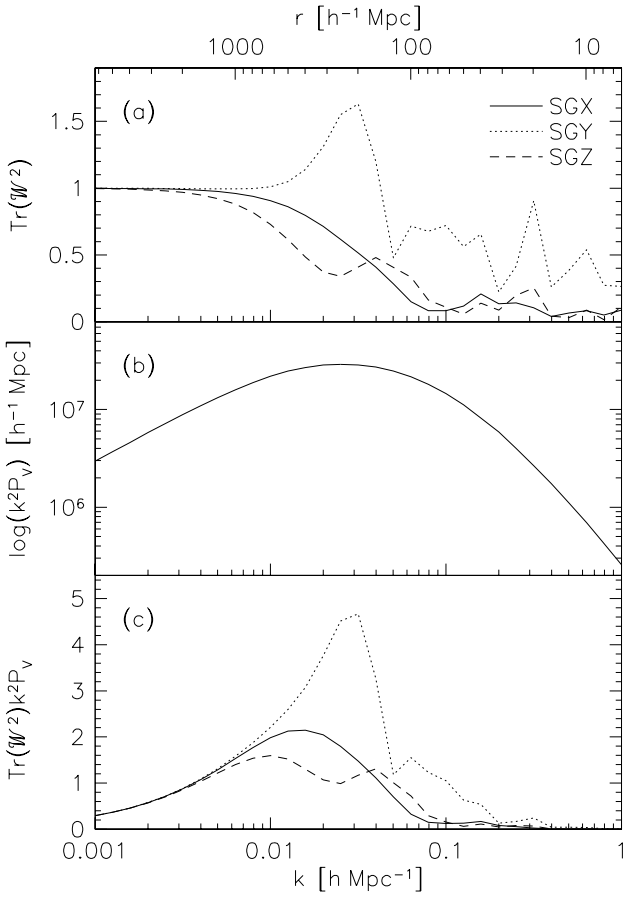

Figure 17. (a) The trace of the squared tensor window function for the EFAR sample along the Supergalactic X, Y and Z axes; (b) the power spectrum for a CDM-like model with Γ=0.25 and σ_8=1.0; and (c) the contributions of different scales to the covariance in the measured bulk velocity, given by the product of the power spectrum and the squared tensor window function.

where σ_1, σ_2 and σ_3 are the lengths of the axes of the covariance ellipsoid obtained from the eigenvalues of the covariance matrix. The directions of these axes are given by the (orthogonal) eigenvectors of the covariance matrix. For the EFAR sample and our adopted cosmological model, these eigenvalues and eigenvectors (in Supergalactic coordinates) are

$$\begin{array}{ll} \sigma_1 = 454\,\mathrm{km\,s^{-1}} & \boldsymbol{e_1} = (+0.7026, +0.5604, -0.4385)\ , \\ \sigma_2 = 309\,\mathrm{km\,s^{-1}} & \boldsymbol{e_2} = (+0.5679, -0.0703, +0.8201)\ , \\ \sigma_3 = 185\,\mathrm{km\,s^{-1}} & \boldsymbol{e_3} = (-0.4287, +0.8253, +0.3676)\ . \end{array} \quad (19)$$

The corresponding directions in Galactic coordinates are $\boldsymbol{e_1}$=(172.6°,+30.6°), $\boldsymbol{e_2}$=(82.0°,+1.2°), and $\boldsymbol{e_3}$=(350.0°,+59.4°). We therefore find an expectation value for the amplitude of the bulk flow of 619 km s^{-1}, so that the observed value is not much larger than that expected from our model, as the χ^2 statistic indicates. It is worth noting that the expected bulk flow amplitude is strongly dominated by the 'noise' term in the covariance matrix. For our adopted cosmological model in the absence of noise, we would expect to measure a bulk flow amplitude from the EFAR sample of only 355 km s^{-1}, whereas in the absence of any cosmological velocities, the noise in our measurement would still lead us to expect a bulk flow amplitude of 553 km s^{-1}.

We obtain a smaller upper limit on the bulk motion we if consider only the component of the bulk flow along the minimum-variance axis of the covariance ellipsoid. Unsurprisingly, this axis, $\boldsymbol{e_3}$=(350.0°,+59.4°), is just 20° away from the median axis of the 50 clusters in the peculiar velocity sample, $\langle(l,b)\rangle$=(7°,+42°). The expected bulk flow amplitude along this axis is 147 km s^{-1} (124 km s^{-1} from noise alone, 76 km s^{-1} from model alone), while the maximum likelihood estimate of the observed bulk motion is 269 km s^{-1}. Since σ_3=185 km s^{-1}, this gives χ^2=2.11 with 1 degree of freedom, implying that the observed bulk motion in this direction is consistent with the model at the 15% confidence level.

Thus there is no evidence that the bulk motion of the EFAR sample is inconsistent with a cosmological model having a CDM-like power spectrum with Γ=0.25 and σ_8=1.0, consistent with the best current determinations. In fact, repeating this analysis, we find that the observations are consistent with a wide range of cosmological models, including both standard CDM and open, low-density CDM models.

We can also ask to what extent the EFAR sample is capable of testing whether the bulk motions measured by Lauer & Postman (1994), SMAC (Hudson et al. 1999) and LP10K (Willick 1999) are consistent with the velocity field model. To do so we use the χ^2 statistic computed according to equation 17, inserting the EFAR covariance matrix for $\boldsymbol{R}$ and the observed Lauer & Postman, SMAC or LP10K bulk motions for $\boldsymbol{U}$. If the EFAR bulk motion had been found to be identical to the SMAC result, it would have been consistent with the velocity field model at the 25% level; if it had been found to be identical to the LP10K result it would have been consistent with the model at the 9% level. However a bulk motion identical to the Lauer & Postman result would have been rejected at the 0.09% level. Hence, as expected, the directionality of the EFAR sample means that while it would have provided a strong indication of an inconsistency with the model if the Lauer & Postman result had been recovered, recovery of the SMAC or LP10K results would not have implied a problem with the model.

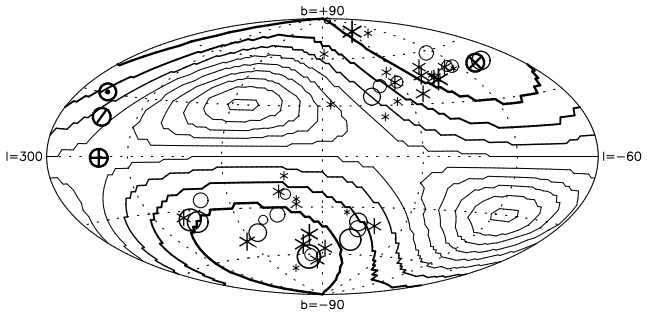

Figure 18. Contour plots of the bulk motion amplitude, in each direction on the sky, that would be rejected at the 1% level or better by the EFAR sample. The assumed power spectrum is CDM-like, with Γ = 0.25 and σ_8=1.0, and the rms thermal motions of the clusters is assumed to be σ_*=250 km s^{-1}. The EFAR clusters with positive (negative) peculiar velocities are indicated by asterisks (circles). Other symbols show the directions with respect to the CMB frame of the Local Group dipole (⊙), the Lauer & Postman (1994) dipole (⊗), the SMAC (Hudson et al. 1999) dipole (⊕), and the LP10K (Willick 1999) dipole (⊘). The contours run in steps of 100 km s^{-1} from 700 km s^{-1} to 1500 km s^{-1}, with the lowest contour being the thickest.

We can generalise this analysis to illustrate how the directionality of the EFAR sample affects the constraints it could place on observed bulk motions in different directions. Figure 18 shows, in each direction on the sky, the amplitude of the observed bulk motion that would be rejected as inconsistent with the velocity field model at the 1% confidence level using equation 17.

It is important to emphasise that although it would not have been surprising, under this model, to have recovered the SMAC motion from the EFAR sample, in fact the tests of the previous section indicated that the actual motions recovered from the EFAR sample are highly inconsistent with a pure SMAC bulk flow. As already noted, however, because those tests do not use a full velocity field model and do not account for the window function of the sample, they will tend to over-estimate the degree of inconsistency. The best test is a simultaneous consistency check between both datasets and the model (Watkins & Feldman 1995), determining the joint probability of deriving both the observed EFAR bulk motion from the EFAR sample and the observed SMAC motion from the SMAC sample under the assumptions of the velocity field model. This type of test has already been carried out for the SMAC sample with respect to various other samples by Hudson et al. (2000), who find consistency with all the other peculiar velocity surveys with the possible exception of Lauer & Postman, and a marginal conflict with a flat ΛCDM model similar to that used here. Once the SMAC peculiar velocities have been published, a similar test can be carried out to check the consistency of the EFAR and SMAC survey results.

7 CONCLUSIONS

We have measured peculiar velocities for 84 clusters of galaxies in two large, almost diametrically opposed, regions at

distances between 6000 and 15000 km s^{-1}. These velocities are based on Fundamental Plane (FP) distance estimates for early-type galaxies in each cluster. We fit the FP to the best-studied 29 clusters using a maximum likelihood algorithm which takes account of both selection effects and measurement errors and yields FP parameters with smaller bias and variance than other fitting procedures. We obtain a best-fit FP with coefficients consistent with the best existing determinations. Apparent differences in the FPs obtained in previous studies can be reconciled by allowing for the biases imposed by the various fitting methods. We then fix the FP parameters at their best-fit values and derive distances for the whole cluster sample. The resulting peculiar velocities show no evidence for residual systematic errors, and, for the small numbers of clusters in common, are consistent with those measured by other authors.

We have examined the bulk motion of the sample regions using the 50 clusters with the best-determined peculiar velocities. We find the bulk motions in both regions are small, and consistent with zero at about the 5% level. We use both direct χ^2 comparison and the more sophisticated window function covariance analysis developed by Kaiser (1988) and Feldman & Watkins (1994, 1998) to compare our result with the predictions of standard cosmological models and the results of other studies. We find that the bulk motion of our sample is consistent (at about the 10% level) with the prediction of a ΛCDM model with parameters Γ=0.25, σ_8=1.0 and h=0.7; indeed the motion is consistent with most cosmological models having parameters that are broadly consistent with the observed shape and normalisation of the galaxy power spectrum.

We examine whether our results can be reconciled with the large-amplitude bulk motions on similar scales found in some other studies. Our sample lies close to the direction of the large-amplitude dipole motion claimed by Lauer & Postman (1994), so that we are able to make an effective test of the bulk motion in this direction. We find that a pure Lauer & Postman bulk motion is inconsistent with our data at the 0.2% confidence level. This strong rejection of the Lauer & Postman result is supported by the window function covariance analysis. We find an even stronger inconsistency between the EFAR peculiar velocities and the result of the SMAC survey (Hudson et al. 1999), with a pure SMAC bulk motion ruled out at the 0.04% confidence level. This is a surprisingly strong result, given that the main axis of the EFAR sample lies at a large angle to the direction of the SMAC dipole. It will be important to carry out a simultaneous consistency check of both datasets with a full velocity field model using the generalised covariance analysis described by Watkins & Feldman (1995) and Hudson et al. (2000).

To summarise current observations of bulk motions on scales larger than 6000 km s^{-1}: (i) The EFAR and SCII (Dale et al. 1999a) surveys find small bulk motions, close to the predictions of cosmological models that are constrained to be consistent with other large-scale structure observations. (ii) The SMAC survey (Hudson et al. 1999) finds a bulk motion with a much larger amplitude. However a full accounting for the uncertainties and window function of the survey shows that it is in fact only marginally inconsistent with the models (at about the 2σ level; Hudson et al. 2000). (iii) The LP10K survey finds a bulk motion very similar to the SMAC dipole, but the smaller sample size means that the uncertainties are larger and consequently the result is not inconsistent. (iv) The Lauer & Postman (1994) result *is* inconsistent with such models at the 3–5% level (Feldman & Watkins 1994). However it is also inconsistent with the EFAR results (at the 0.2% confidence level) and with the other surveys combined (at the 0.6% level; Hudson et al. 2000), and therefore should be treated with reserve. We conclude that existing measurements of large-scale bulk motions provide no significant evidence against standard models for the formation of structure.

ACKNOWLEDGEMENTS

This work was partially supported by NSF Grant AST90-16930 to DB, AST90-17048 and AST93-47714 to GW, and AST90-20864 to RKM. RPS was supported by DFG grants SFB 318 and 375. The collaboration benefitted from NATO Collaborative Research Grant 900159 and from the hospitality and financial support of Dartmouth College, Oxford University, the University of Durham and Arizona State University. Support was also received from PPARC visitors grants to Oxford and Durham Universities and a PPARC rolling grant 'Extragalactic Astronomy and Cosmology in Durham'.

REFERENCES

Abell G.O., Corwin H.G., Jr, Olowin R.P., 1989, ApJS, 70, 1
Baugh C.M., Efstathiou G., 1993, MNRAS, 265, 145
Burstein D., Heiles C., 1982, AJ, 87, 1165
Burstein D., Heiles C., 1984, ApJS, 54, 33
Coles P., Lucchin F., 1995, Cosmology: The Origin and Evolution of Cosmic Structure, J.Wiley & Sons, Chichester
Colless M.M., 1995, AJ, 109, 1937
Colless M.M., Burstein D., Wegner G., Saglia R.P., McMahan R., Davies R.L., Bertschinger E., Baggley G., 1993, MNRAS, 262, 475
Colless M.M., Burstein D., Davies R.L., McMahan R., Saglia R.P., Wegner G., 1999, MNRAS, 303, 813 (Paper V)
Courteau S., Willick J.A., Strauss M.A., Schlegel D., Postman M., 2000, in Cosmic Flows: Towards an Understanding of Large-Scale Structure, eds Courteau S., Strauss M.A., Willick J.A., ASP Conf. Series, in press, astro-ph/9909385
da Costa L.N., Bernardi M., Alonso M.V., Wegner G., Willmer C.N.A., Pellegrini P.S., Maia M.A.G., Zaroubi S., 2000, ApJL, submitted, astro-ph/9912225
Dale D.A., Giovanelli R., Haynes M.P., Campusano L.E., Hardy E., Borgani S., 1999a, ApJ, 510, L11
Dale D.A., Giovanelli R., Haynes M.P., Campusano L.E., Hardy E., 1999b, AJ, 118, 1489
Davis D.S., Bird C.M., Mushotzky R.F., Odewahn S.C., 1995, ApJ, 440, 48
Dekel A., Eldar A., Kolatt T., Yahil A., Willick J.A., Faber S.M., Courteau S., Burstein D., 1999, ApJ, 522, 1
Dekel A., 2000, in Cosmic Flows: Towards an Understanding of Large-Scale Structure, eds Courteau S., Strauss M.A., Willick J.A., ASP Conf. Series, in press, astro-ph/9911501
Djorgovski S., Davis M., 1987, ApJ, 313, 59
Dressler A., Lynden-Bell D., Burstein D., Davies R.L., Faber S.M., Terlevich R.J., Wegner G., 1987, ApJ, 313, 42
Feldman H.A., Watkins R., 1994, ApJ, 430, L17
Feldman H.A., Watkins R., 1998, ApJ, 494, L129
Gibbons R.A., Fruchter A.S., Bothun G.D., 2000, preprint, astro-ph/9903380

Giovanelli R., Haynes M.P., Freudling W., Da Costa L.N., Salzer J.J., Wegner G., 1998a, ApJ, 505, L91
Giovanelli R., Haynes M.P., Salzer J.J., Wegner G., Da Costa L.N., Freudling W., 1998b, AJ, 116, 2632
Guzmán R., Lucey J.R., Bower R.G., 1993, MNRAS, 265, 731
Huchra J.P., Geller M., Clemens C., Tokarz S., Michel A., 1992, Bull.C.D.S., 41, 31
Hudson M.J., Lucey J.R., Smith R.J., Steel J., 1997, MNRAS, 291, 488
Hudson M.J., Smith R.J., Lucey J.R., Schlegel D.J., Davies R.L., 1999, ApJ, 512, 79L
Hudson M.J., Smith R.J., Lucey J.R., Schlegel D.J., Davies R.L., 2000, in Cosmic Flows: Towards an Understanding of Large-Scale Structure, eds Courteau S., Strauss M.A., Willick J.A., ASP Conf. Series, in press, astro-ph/9909307
Jackson R., 1982, PhD thesis, Univ. California, Santa Cruz
Jørgensen I., Franx M., Kjærgaard P., 1996, MNRAS, 280, 167
Jørgensen I., 1997, MNRAS, 288, 161
Kaiser N., 1988, MNRAS, 231, 149
Kogut A., Lineweaver C., Smoot G.F., Bennett C.L., Banday A., Boggess N.W., Cheng E.S., de Amici G., Fixsen D.J., Hinshaw G., Jackson P.D., Janssen M., Keegstra P., Loewenstein K., Lubin P., Mather J.C., Tenorio L., Weiss R., Wilkinson D.T., Wright E.L., 1993, ApJ, 419, 1
Lauer T.R., Postman M., 1994, ApJ, 425, 418
Lucey J.R., Bower R.G., Ellis R.S., 1991, MNRAS, 249, 755
Müller K.R., 1997, PhD thesis, Dartmouth College
Müller K.R., Freudling W., Watkins R., Wegner G., 1998, ApJ, 507, L105
Müller K.R., Wegner G., Raychaudhury S., Freudling W., 1999, A&AS, 140, 327
Pahre M.A., Djorgovski S., de Carvalho R.R., 1998, AJ, 116, 1606
Pierce M.J., Tully R.B., 2000, in Cosmic Flows: Towards an Understanding of Large-Scale Structure, eds Courteau S., Strauss M.A., Willick J.A., ASP Conf. Series, in press
Press W.H., Flannery B.P., Teukolsky S.A., Vetterling W.T., 1986, Numerical Recipes, Cambridge University Press, Cambridge
Riess A.G., 2000, in Cosmic Flows: Towards an Understanding of Large-Scale Structure, eds Courteau S., Strauss M.A., Willick J.A., ASP Conf. Series, in press, astro-ph/9908237
Saglia R.P., Bertschinger E., Baggley G., Burstein D., Colless M.M., Davies R.L., McMahan R., Wegner G., 1993, MNRAS, 264, 961
Saglia R.P., Burstein D., Baggley G., Bertschinger E., Colless M.M., Davies R.L., McMahan R., Wegner G., 1997a, MNRAS 292, 499 (Paper III)
Saglia R.P., Bertschinger E., Baggley G., Burstein D., Colless M.M., Davies R.L., McMahan R., Wegner G., 1997b, ApJS, 109, 79 (Paper IV)
Saglia R.P., Colless M.M., Burstein D., Davies R.L., McMahan R., Wegner G., 2000, MNRAS, in prep (Paper VI)
Saunders W., Branchini E., Teodoro L., Heavens A., Taylor A., Valentine H., D'Mellow K., Oliver S., Keeble O., Rowan-Robinson M., Sharpe J., Maddox S., McMahon R., Efstathiou G., Sutherland W., Tadros H., Ballinger W., Schmoldt I., Frenk C., White S.D.M., in Cosmic Flows: Towards an Understanding of Large-Scale Structure, eds Courteau S., Strauss M.A., Willick J.A., ASP Conf. Series, in press, astro-ph/9909190
Schlegel D.J., Finkbeiner D.P., Davis M., 1998, ApJ, 500, 525
Scodeggio M., Giovanelli R., Haynes M.P., 1997, AJ, 113, 101
Sutherland W., Tadros H., Efstathiou G., Frenk C.S., Keeble O., Maddox S.J., McMahon R.G., Oliver S., Rowan-Robinson M., Saunders W., White S.D.M., 1999, MNRAS, 308, 289
Tonry J.L., Blakeslee J.P., Ajhar E.A., Dressler A., 2000, ApJ, submitted, astro-ph/9907062
Watkins R., Feldman H.A., 1995, ApJ, 453, L73
Watkins R., 1997, MNRAS, 292, L59
Wegner G., Colless M.M., Baggley G., Davies R.L., Bertschinger E., Burstein D., McMahan R., Saglia R.P., 1996, ApJS, 106, 1 (Paper I)
Wegner G., Colless M.M., Burstein D., Saglia R.P., McMahan R., Davies R.L., Baggley G., 1999, MNRAS, 305, 259 (Paper II)
Wegner G., da Costa L.N., Alonso M.V., Bernardi M., Willmer C.N.A., Pellegrini P.S., Rite C., Maia M., 2000, in Cosmic Flows: Towards an Understanding of Large-Scale Structure, eds Courteau S., Strauss M.A., Willick J.A., ASP Conf. Series, in press, astro-ph/9908354
Weinberg S., 1972, Gravitation and Cosmology, Wiley, New York
Willick J.A., 1999, ApJ, 522, 647
Zabludoff A.I., Franx M., Geller M.J., 1993, ApJ, 419, 47